AN ABSTRACT OF THE THESIS OF

Guoheng Ma for the degree of Master of Science in Chemical Engineering presented on March 14, 2016.

Title: Synthesis of Plasmonic-Enhanced Metal-Organic Framework Thin Films and their Infrared Sensing Application.

Abstract approved: _____

Chih-Hung Chang

Transparent and electrically conductive metal oxide nanoparticles have attracted much attention, and can be used to improve the performance of solar cells, transparent electrode materials, and gas sensor technology. Specifically, indium tin oxide (ITO) nanocrystals (NCs) are potentially useful nanomaterials, having technological applications in enhanced sensitivity of optical spectroscopy due to their localized surface plasmon resonance (LSPR). Metal organic frameworks (MOFs) are a class of novel inorganic-organic hybrid materials with varied structure and tunable functions that award MOFs high capability of gas absorption. In this research we combine ITO NCs with highly porous Cu-BTC MOF in a sandwich-structured thin film with an end-goal to enhance the IR absorption of CO_2 in the NIR range.

High quality mono-dispersed organic-ligand-capped colloidal ITO NCs are

synthesized. The hydrophobic capping agents stabilize the NCs in nonpolar solvents and prevent their aggregation, but are not propitious for Cu-BTC MOF growing on the surface. The capping reagent were modified from a hydrophobic to a hydrophilic by using 3-Aminopropyl triethoxysilane (APTES) which provide an $-NH_2$ terminated functional group that allows for the growth of MOF crystals. Based on (3-Aminopropyl)triethoxysilane (APTES) capped ITO (APTES-ITO), a sandwich-structured film made by APTES-ITO films and Cu-BTC MOF films was fabricated on glass. The sensing capability of CO_2 was measured in the NIR range. No enhancement of signal intensity was observed. Several reasons were suggested for the no enhancement of IR absorption including the presence of water; the presence of surface ligands on ITO NCs; and the non-optimum gas cell design.

Synthesis of Plasmonic-Enhanced Metal-Organic Framework Thin Films and their Infrared Sensing Application

by

Guoheng Ma

A THESIS

submitted to

Oregon State University

in partial fulfillment of
the requirements for the
degree of

Master of Science

Presented March 14, 2016
Commencement June 2016

Master of Science thesis of Guoheng Ma presented on March 14, 2016

APPROVED:

Major Professor, representing Chemical Engineering

Head of the School of Chemical, Biological, and Environmental Engineering

Dean of the Graduate School

I understand that my thesis will become part of the permanent collection of Oregon State University libraries. My signature below authorizes release of my thesis to any reader upon request.

Guoheng Ma, Author

ACKNOWLEDGEMENTS

First of all, I would like to thank Dr. Chih-hung Chang for his support and guidance in accomplishing this research and completing the writing process. I am extremely grateful to the chance to join Dr. Chang's group. The past two years of studying and working in his group have been an important and meaningful experience for my life.

I would like to express my gratitude to Dr. Ki-joong Kim whose advice, suggestion and teaching have helped me tremendously through my research and thesis completion. I feel so lucky to have a chance to work and study with him. His guidance in experimental design, instrument operation and data explanation helped me to push my research forward.

I would like to thank Fei Teng in the school of MIME, who gave me professional guidance in XRD characterization.

I would also like to express my thanks to all my group members. I would like to thank Yujing Zhang for sharing her knowledge on MOF growth. I would like to thank Changqing Pan for his training on instrument operation. I would like to thank Zheng Fang for his help in O_2 plasma treatment, and to Yujuan He, Zhongwei Gao, Dick Chiu, Jenna Y. Gorecki, Michele David and Shujie Li for their help and wonderful time spending together.

Finally, I am extraordinarily thankful for Xuan Jiao for her loyal love, innumerable encouragement and selfless dedication. I am so lucky to meet her here in Corvallis.

TABLE OF CONTENTS

Page

LIST OF FIGURES

Figure Page

LIST OF FIGURES (Continued)

Figure Page

LIST OF FIGURES (Continued)

Figure Page

LIST OF TABLES

Table Page

1. Introduction

1.1 Introduction of Metal Organic Frameworks

Metal organic frameworks (MOFs) are a class of novel inorganic-organic hybrid materials made up of metal ions and coordinated organic linkers [1-3]. Through changing different metal ions and organic linkers, MOFs can have varied structure and tunable functions that award MOFs plentiful potential applications. Gases can be stored within MOF's inner pores by a rapid physisorption and fast and easy removal by exposing to vacuum or flowing inert gases. In the past decade, MOFs have attracted substantial attentions; and thousands of MOFs materials have been synthesized and reported [2]. The coordination between the didentate- or polydentate- negatively-charged organic likers and positively-charged metal ions yield distinctive properties, such as structurally ordered crystal, large surface/mass ratio, well-regulated pores and functions based on the unique structure. These properties make MOFs highly functional materials for storage and separation of small molecules in both gas phase and liquid phase, heterogeneous catalysis loading catalyst in its porous sturcture, support/host materials for other functional materials and working as templates/nanoreactors [4-7].

1.2 IR sensing

Recently, various gas sensing approaches using nanoporous MOF thin films have been reported [7-10]. These MOF-based sensors using different working principles including solvatochromism/vapochromism, photoluminescence, radioluminescence, interferometry, localized surface plasmon resonance, impedance spectroscopy and electromechanical sensing. Although MOF-based sensors are excellent for detecting many small gases molecules, there are some challenges that need to be overcome. Lack of signal transduction methods is one of the most significant challenges except luminescence MOF. No observable sensing signal could be displayed without a signal transduction system. Another area needed for improvement is selectivity. MOF materials couldn't selectively respond to a single analyte in a mixture that contains various adsorbing components.

Infrared (IR) gas sensing is a widely used optical gas sensing technology. It plays an important role in quantitative detection and molecular structure identification. As a type of optical sensing method, IR sensing has many advantages, such as short response time, high selectivity and stability. The principle of IR-source gas sensor is working based on absorption spectroscopy that is a molecular absorption of the radiation at specific wavelengths caused by fundamental molecular vibrations of analyte molecules with unique fingerprints in the IR range. Therefore, IR spectroscopy is very attractive for gas sensing and

identification compared with other methods. However, most commercial IR applications on gas sensors are large and heavy for portable sensing application, and also high cost. In recent years, chip-scale gas sensors based on IR absorption spectroscopy have been created in lab [11,12]. Compared to traditional IR gas sensors, these small on-chip sensors are suitable for a wide range of gases. But there still have restrictions for the application of these sensors. Increasing the low detection sensitivity is the biggest challenge, because most gas molecules do not have strong fingerprint in the absorption spectrum in the Near IR (NIR) wavelength rang (from about 700 nm to 2500 nm). That is why new functional materials and creative engineering processes should be employed on the NIR absorption-detection sensors to increase signal intensity of target gases in the NIR range.

According to Beer-Lambert Law, the transmitted intensity I is described as

$$I = I_0 \times \exp(-\gamma \alpha L), \quad (1)$$

where I_0 is the intensity of incident light, α is the absorption coefficient, L is the optical path length, and γ is the medium-specific absorption factor. For a chip size sensor, L is small; in a free-space system $\gamma = 1$ [13]. Based on equation (1), increase α could directly enhance the IR absorption. Researches have already showed that electric field could induce a strong IR absorption of H_2 [14,15], semiconductor and insulator [16,17], diamond [18] and N_2 [19]. Localized surface plasmonic resonance (LSPR) [9,22,23] of nanoparticles could enhance the electric

field significantly around the surface of nanoparticles, especially at the hot points [9,22].

1.3 Plasmonic effect

Plasmon can be described as an oscillation of free electron density [22]. The plasma frequency of conducting metal oxide in free space is defined as [20],

$$\omega_p = \sqrt{\frac{n_c e^2}{\varepsilon_0 m^*}} \quad (2)$$

Where n_c is the free carrier density; e is elementary charge; ε_0 is dielectric permittivity of free space, and m^* is the effective mass of an electron. Theoretically, each type of plasma has its intrinsic oscillating frequency relating to free carriers, such as charge, density, effective mass, and mobility; and is also associated with size and shape of the materials, composition, ambient environment [21].

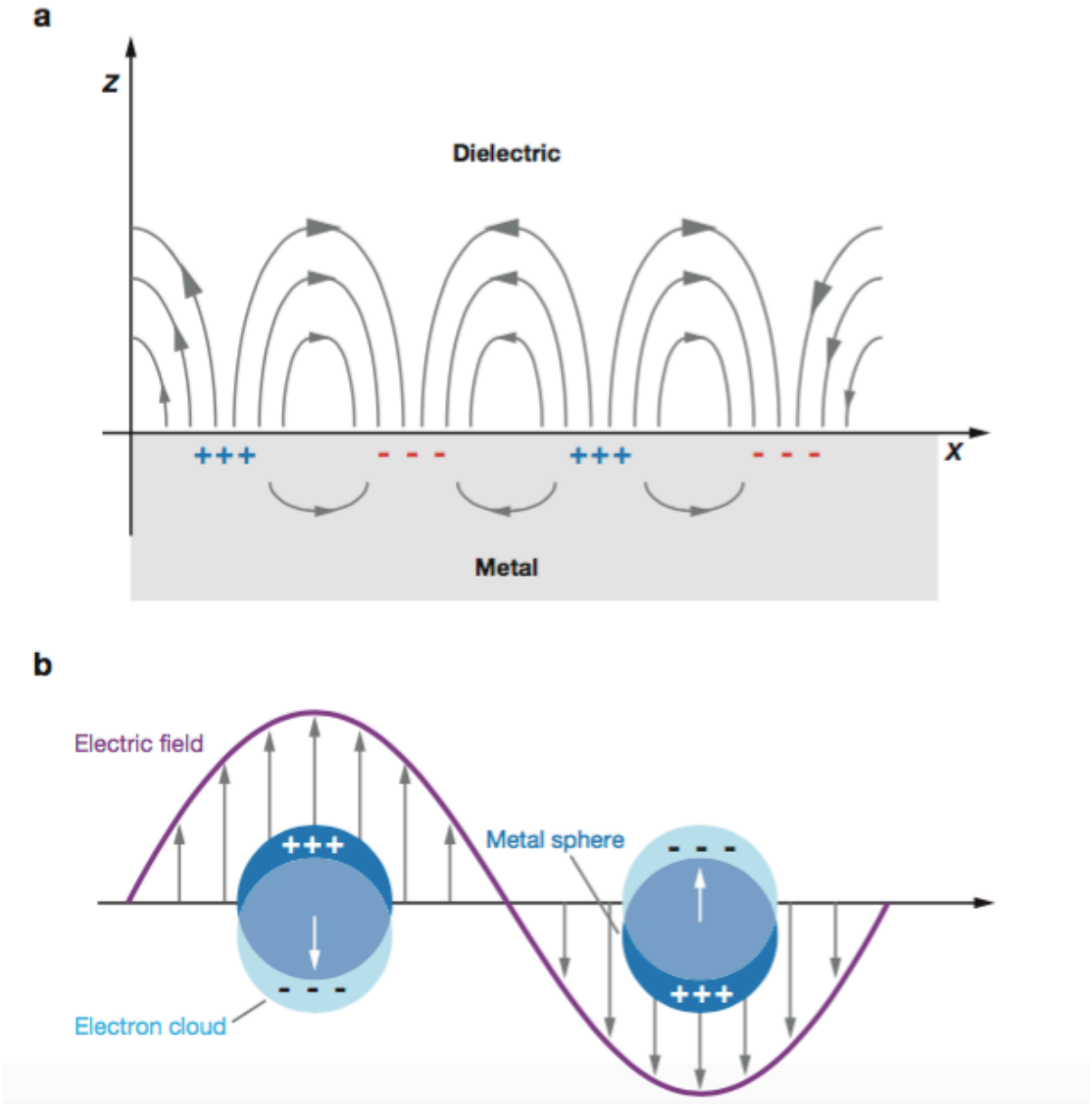

Figure 1. Schematic diagrams of (a) a surface plasmon polariton also called plasmon and propagating and (b) a localized surface plasmon, displaying electron cloud vibration for conducting material sphere particles in affection of electric field. Reproduced from reference [22].

Conducting materials with geometric plane and smooth surface, such as the interface of vacuum and metal/metal oxide, the surface plasmon polaritons appear and propagate along the surface under electromagnetic radiation (*figure 1a*). [22,23] This is the surface plasmon. In the case of Localized Surface Plasmon

(*figure 1b*), incident light interacts with the free carriers in the isolated and small particles leading to oscillation of free carriers density. This polarized oscillation is confined in a certain small space without propagation. When the frequency of incident radiation (light) is equal to the intrinsic oscillating frequency, originate a Localized Surface Plasmon Resonance (LSPR) that is a coherent oscillation of the light-excited free electrons confined in a small space, such as a space around conductive nanoparticles (NPs). The interaction of NPs and light allows part of the incident light to be absorbed and scattered. At the same time, LSPR evokes an extremely intensed and highly localized electric fields in the space near surfaces of NPs. This electric field could increase the absorption coefficient in Equation (1). Combining the enhanced electric field and MOF material, which could absorb and concentrate analyte in its highly porous structure, we expect the absorption intensity of analyte could be enhanced by this IR-based sensor.

1.4 Plasmonic material -- Indium Tin Oxide

Indium tin oxide is tin doped indium oxide with the same crystal structure as In_2O_3. The stable and common form of In_2O_3 is cubic bixbyite type In_2O_3 (*c*-In_2O_3) with body-centered cubic crystal structure. Additionally, a metastable corundum-type In_2O_3 (*h*-In_2O_3) with rhombohedral crystal structure could also be obtained at high pressures or temperatures (*figure 2*). [24]

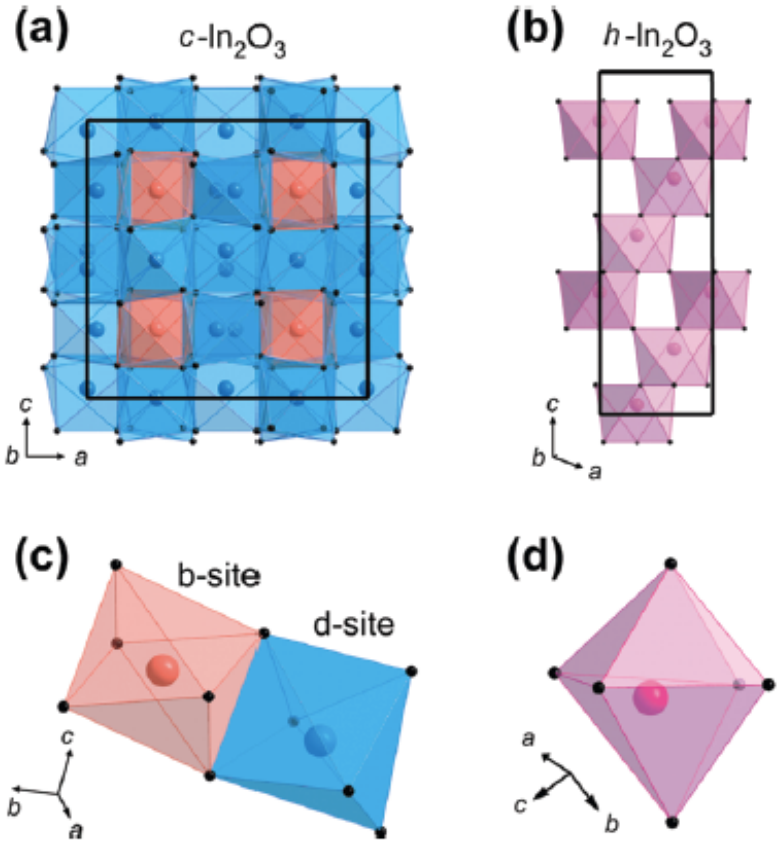

Figure 2. Crystal unit cell of (a) cubic bixbyite-type In_2O_3 (*c*-In_2O_3), and (b) corundum-type In_2O_3 (*h*- In_2O_3). The In^{3+} sites in *c*- In_2O_3 (c) and *h*- In_2O_3 (d). Large-colored spheres are indium atoms and small-black spheres are oxygen atoms. Reproduced from reference [24].

One-fourth of total In^{3+} cations have slightly deformed octahedral coordination (b-sites in *figure 2c*). The other three-fourths of In^{3+} cations have a highly distorted octahedral coordination structure (d-sites in *figure 2c*). Oxygen ions in metastable *h*-In_2O_3 are only hexagonal close-packed; hence only two-thirds of the six-coordinate octahedral spaces are filled by In^{3+} cations. The other one-third octahedral spaces are vacant.

Plasmonic ITO only has the stable crystal structure as cubic bixbyite-type In_2O_3, because the doped-tin atoms replace part of indium atoms from the original

positions without changing crystal structure. Comparing with indium atom, tin atom has one free electron when it is doped in In_2O_3. ITO not only maintains the high visible light transmittance as indium oxide, but also have free electrons which give ITO the properties of conducting and plasmonic effect. Owing to the high optical transparency and excellent electrical conductivity, the transparent and electrically conductive ITO have attracted much attention, and can be used to improve the performance of solar cells [25], transparent electrode materials [26], gas sensor technology [9] and smart window [27]. Here, we are only interested in the plasmonic effect of ITO, but not the electrical property which need a condense ITO film. Hence ITO NCs is employed.

1.5 Plasmonic-enhanced MOF film for NIR sensing

Plasmonic NCs have been used for improving the sensitivity of surface-enhanced infrared absorption (SEIRA) [9, 28-32]. In these SEIRA studies, noble metals such as gold are critically researched [29-32], because the noble metal film could enhance the signals based on monolayer sensitivity. Metal oxide or doped metal oxides such as ITO NCs could also be used as SEIRA materials [9]. The transparent conducting ITO NCs have LSPR in NIR region. Through changing the ratio of tin doping, the LSPR peak wavelength can be easily tuned to match the vibration bands of selected gas molecules in NIR range. Due to free carrier density

changes with gas adsorption in plasmonic materials, the NIR absorption gas sensors based on SEIRA concept is enhanced in selectivity. To further enhance the sensitivity, MOF is employed as a gas accumulation material owing to its unique quality for gas storage. As aforementioned, ITO NCs could only increase the NIR vibration of gas molecules in a region of few nanometers from NCs' surface, because the electric field created by LSPR decays very fast outside NCs. Increasing gas concentration in the effective space of the electric field means the vibration of more gas molecules will be enhanced that should lead to a stronger absorption in the IR spectrum. A MOF and ITO sandwich structure (*figure 3*) massively increases interface between ITO and MOF. With selectively absorb and accumulate large amount of analyte molecules in the highly porous MOF, the sandwich-structure film gas sensor could be used for low concentration gas sensing. Here, we select the MOF, $Cu_3(BTC)_2(H_2O)_3$ (HKUST-1), for CO_2 sensing [7,33]. Because HKUST-1 has ideal property for CO_2 sorption [33-37] and CO_2 has detectable absorption in NIR range.

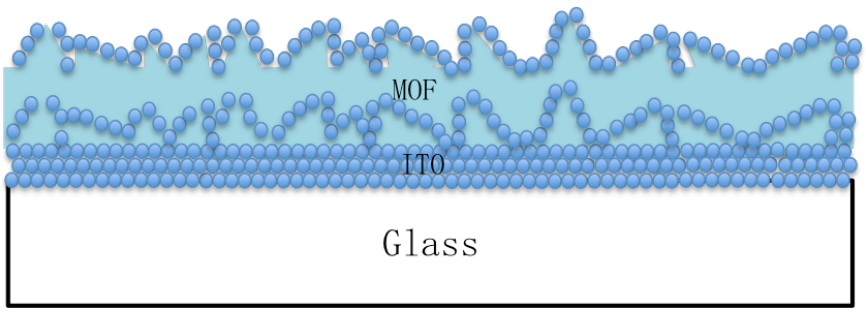

Figure 3. Schematic illustration of the thin film gas sensor with ITO/MOF sandwich structure.

1.6 Fabrication methods of MOF films

Because of the pronounced functionalities of highly porous MOF materials, fabrication of well-defined and highly porous MOF thin films have been developed to produce stable MOF thin films on various kinds of substrates for applications in the fields of sensors and selective membranes, because MOF films bounded on substrate surface normally have larger internal surface area [1]. These substrates are typically metal, metal oxide, glass, or silicon. Most commonly, two major types of methods are used for MOF films formation. One is directly fabricated on the surface of substrates. The other method is synthesizing small MOF particles and subsequently deposit on substrate surface.

Colloidal deposition [38-47] is an easy approach to deposit various classes of MOF crystals on substrates. Monodispersed polyhedral MOFs crystals (*figure 4*), size from nanometers to micrometers, are prepared in colloidal solution through normal solvothermal synthesis. MOF films with tunable thickness could be deposited on solid substrate by simple deposition techniques, e.g. dip coating and spin coating.

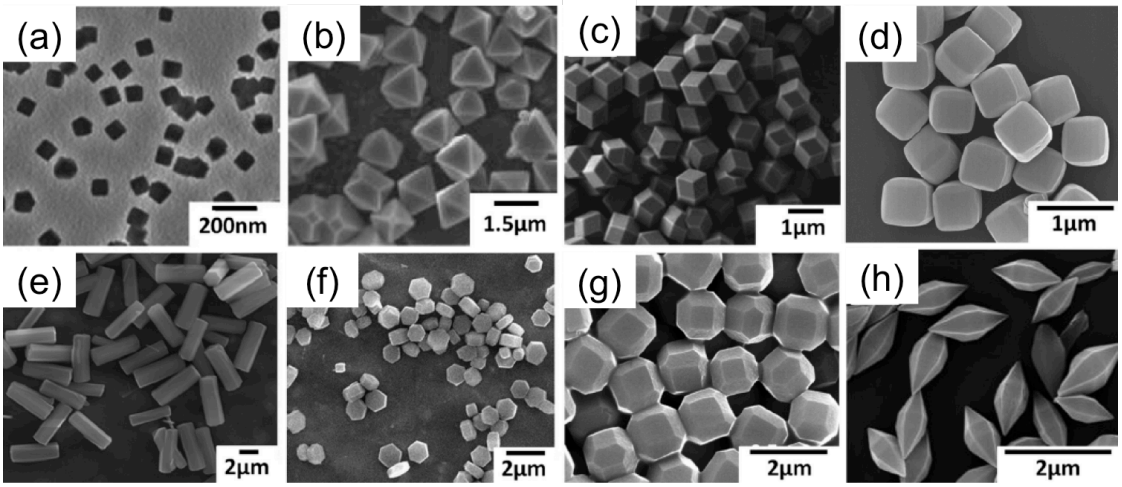

Figure 4. Various shapes of monodisperse colloidal MOFs including (a) cubes, (b) octahedra, (c) rhombic dodecahedra, (d) truncated cubes, (e) hexagonal rods, (f) hexagonal discs, (g) truncated rhombic dodecahedra, and (h) bipyramidal hexagonal prisms. Reproduced from reference [47].

As the particles size and shape are regulated, the MOF film could be formed with desired thickness and controlled spatial arrangements of MOF crystals. But the MOF films prepared using this method are not firmly attached on the substrate and not highly oriented.

The direct film formation can be simply accomplished by placing substrates in a reactor with MOF precursors solution. Direct growth in precursors solution is one of the most widely used methods for MOF film fabrication. Solvothermal method [48-51] is straightforward to prepare well-defined MOF films on substrates with self-assembled monolayers (SAMs) in hot solution containing metal and organic linkers precursors. Microwave-assisted solvothermal synthesis [52,53] could reduce growth time of MOF film from tens of hours to few seconds by heating the conductive layer on substrate by microwave irradiation. In addition,

electrochemical synthesis [54,55] and gel-layer [56] synthesis had also been created to deposit MOF films on substrates in solution base.

Layer-by-layer (LBL) method is another direct MOF films deposition method, but it is in contrast to the above-mentioned synthesis protocols that all the precursors are mixed and react in solution. In the LBL case, substrate is sequential immersed into solutions of metal and organic precursors (*figure 5*) leading to one molecular layer or ionic layer growth through each step [57]. Rinsing with solvent is following with each individual immersion step to remove unreacted components.

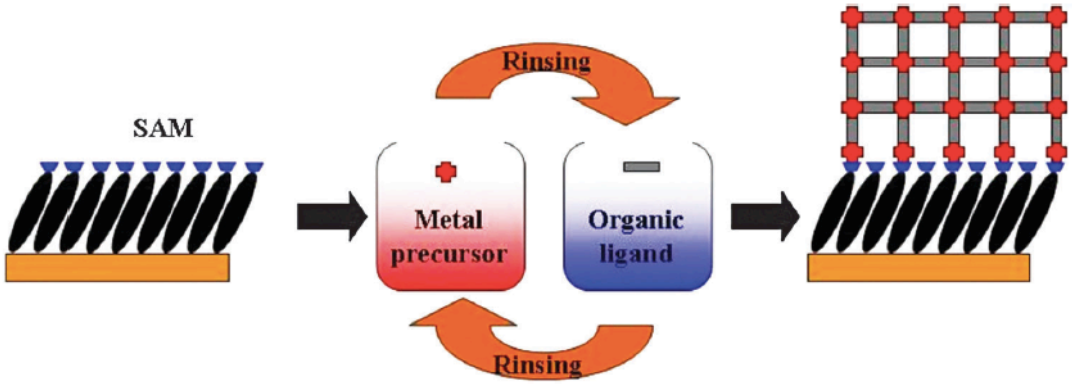

Figure 5. Schematic diagram for the LBL method for the growth of the MOFs on substrates functionalized with SAMs. Reproduced from reference [57].

MOF will nucleate and grow on the SAM layer which is coated on the substrate, and be firmly anchored by the functional groups of SAM. With a number of different SAMs terminations including -OH, -COOH, pyridine and etc., LBL is successfully used for the formation of many different types of MOF films with highly ordered

and homogeneous morphology of crystalline structure. [1, 50, 51, 57]

1.7 Synthesis methods of ITO nano cystals (NCs)

Normally, dc and rf magnetron sputtering, with an In-Sn alloy or an In_2O_3-SnO_2 as sputtering targets, are the fabricated method for high quality ITO film with highest available transmissivity for visible light and lowest electrical resistivity [58]. However, gas-phase sputtering deposition is a high-energy cost, time consuming, low production yield method [59, 60] and also inconvenient to control the patterns and the materials of the substrates. The vital defect is that a density and continuous layer of ITO doesn't have LSPR to create hot points where the electric field is enhanced thousands of times [9]. Due to these weak points, we focus our interest on ITO nanoparticles. After dispersing in appropriate solvent, ITO NPs are easily coated on flexible substrates with drop casting, spin coating and inject printing technology [61].

1.7.1 Co-precipitation method

The co-precipitation method [62-66] synthesizes ITO NPs through annealing precipitated Indium-tin hydroxide formed by precipitating the solution of indium chloride and tin chloride at a certain pH adjusted by ammonia. Co-precipitation process has been applied in many fields because of the advantages, such as

controllable product purity, homogeneity, physical properties and particles' shapes, easily operation, simply instruments and cheap chemicals. It is mentionable that the shapes of product can be changed flexibly through changing the solvent in the co-precipitation process. For example, when water is used as the solvent, polyhedral NPs (*figure 6b*) are formed [62,64-66]. When ether is employed as solvent, the shapes of produced ITO are nanowires (*figure 6a*) and nanorods (*figure 6c*). [62]

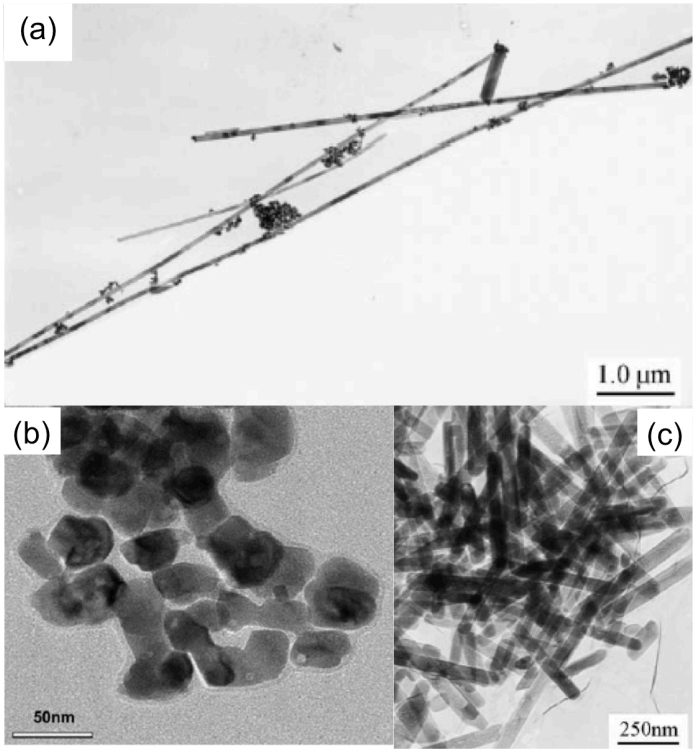

Figure 6. TEM images of (a) nanowires, (b) polyhedral and (c) nanorods ITO synthesized through co-precipitation method. (a) and (c) reproduced from reference [63]; (b) reproduced from reference [62]

In addition, emulsion technique [67] is used to develop the co-precipitation method. In this improved method, precursor is obtained from the precipitation of emulsion containing indium chloride and tin chloride solution and high ratio of 2-butanol or 2-propanol. Spheroidal ITO NPs without any surfactant are prepared from calcination of the dried precursors at a temperature as low as 250°C.

1.7.2 Solvothermal method

The solvothermal approach is a liquid-phase synthesis method. Compared with co-precipitation method, this synthetic method could provide controllable procedures for the nucleation and growth of nano particles in liquid solution. Solvothermal method usually contains creating suspension of metal precursors in polar solvent and successive thermal treatment at high temperature and pressure.

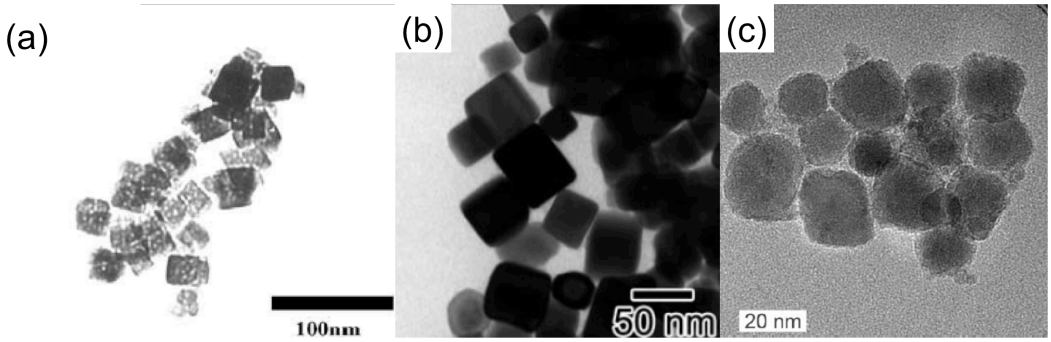

Figure 7. TEM images of cubic ITO NPs (a) and (b) are synthesized through solvothermal method calcining in 250 °C in ethylene glycol; (C) is the ITO NPs from one-pot method. (a) reproduced from reference [68] (b) reproduced from reference [69]. (c) reproduced from reference [70].

Lee and Choi [68] synthesized cubic ITO NPs (*figure 7a*) through the solvothermal method starting from aqueous solution containing indium and tin precursors. Precipitates were formed by adding ammonia and redispersed in polar solvent, such as ethylene glycol, polyethylene glycol and ethanol. ITO nano particles were generated by calcining the solution under 250 °C. Similarly, Sasaki and coworkers [69] synthesized cubic ITO NPs (*figure 7b*) through a one-pot solvothermal procedure, which combined the co-preipitation, nucleation and growth in the same solution. Feldmann and coworkers [70] also synthesized ITO NPs (*figure 7c*) through a one-pot synthesis approach including formation of hydroxide particles in noncoordinating ionic liquids and a subsequent microwave heating under reduced pressure.

1.7.3 Sol-gel method

The sol-gel method is a facile technique for ITO film fabrication with advantages, such as possible deposition onto complex-shaped substrates, easy control of doping level and relatively cheap starting materials. A crucial and representative step in sol-gel synthesis is formation of metal alkoxide sol-gel. Crystalized ITO NPs (*figure 8*) could be generated through thermal treatment of the sol-gel solution and annealing the production of the thermal derived sol-gel solution [71,72]. ITO film could be directly fabricated by annealing deposition

coating of the solution on heat-resistant substrates [73]. However, this method also suffers several problems, such as annealing treatment at high temperature and widespread particle agglomeration.

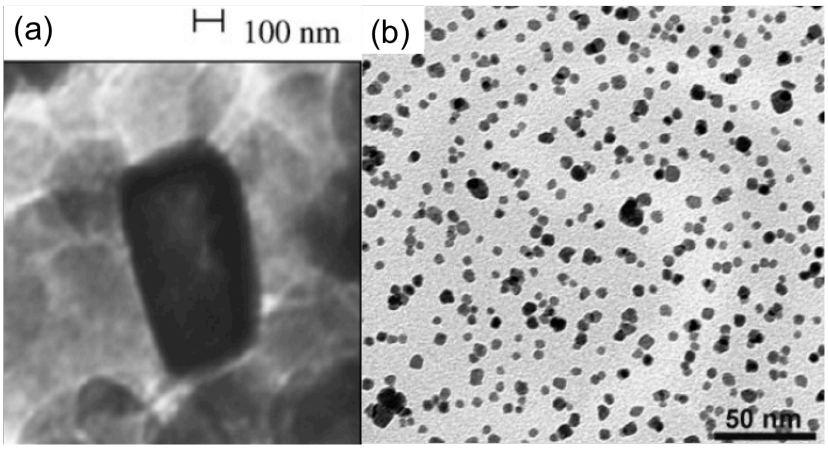

Figure 8. TEM images of ITO NPs synthesized through sol-gel method. (a) Reproduced from reference [71]; (b) reproduced from reference [72].

1.7.4 Nonaqueous thermolysis reactions

Although it has been demonstrated that the above-mentioned thermolysis methods are powerful to prepare ITO NPs, two obvious disadvantages limit the NPs to be applied. The first is the wide size distribution. Particle size is directly related with properties of particles. Wide size distribution may lead non-homogeneity of the product formed by the NPs, such as the thickness and roughness of film, electrical conductivity, reflectivity in different directions, and etc. The other disadvantage is lack of surface capping agents. Without enough surface

adsorbed surfactants, these NPs couldn't stably suspend in most liquid solutions. The unstable suspension usually leads to agglomeration in a process of making film, such as spin coating, dip coating and inkjet printing methods. Consequently, the expected ITO NPs should be narrow-size-distributed and unagglomerated for film fabrication.

In the past few decades, many ITO-synthetic approaches based on thermal decomposition have been created because of their many advantages, such as high crystallinity and monodispersity of the synthesized NPs, high dispersion ability in organic solvents and easily tuned ratio of metal atoms. Typically, these synthetic methods performed the hydrolysis reactions of organometallic compounds and metal-surfactant complexes in hot organic solution at high temperature with the protection of inert gas.

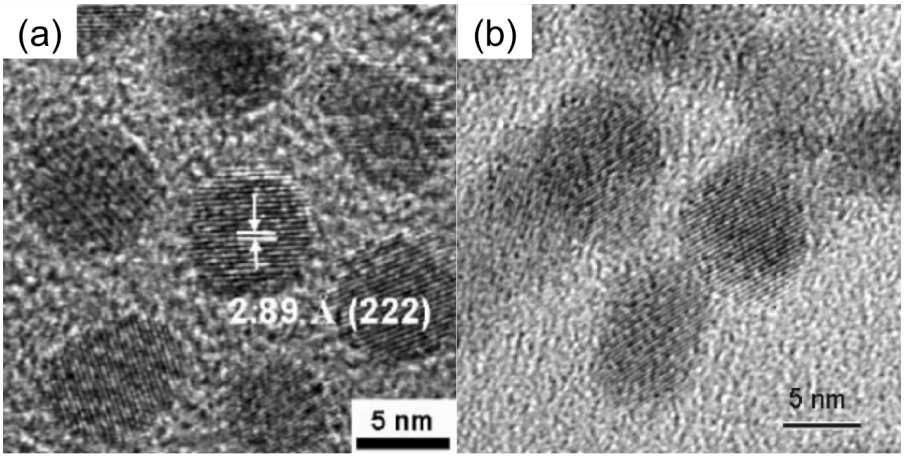

Figure 9. TEM images of ITO NCs synthesized through one-pot method. (a) reproduced from reference [74]; (b) reproduced from reference [75].

To date, two branches have been extended from this synthetic method. One is one-pot method, and the other is hot-injection method. Researchers synthesis ITO NPs (*Figure 9*) based on one pot method [74, 75] started from adding all the chemicals including metal precursors, organic solvent and surface capping agents into one reactor. Water molecules are created through a condensation reaction between carboxylic acid and amine, and then NPs will be generated during a hydrolysis reaction between carboxylate precursors and water. Choi and coworkers [74] create a simple one-pot method that directly decomposed indium acetylacetonate and tin bis-acetylacetonate di-chloride in oleylamine. Here, oleylamine works as both solvent and capping agent. Additionally, a relatively complex one-pot method was published by Sun [75] and Masayaki [76]. Both introduced indium and tin (IV) precursors in a reactor with octadecene, oleylamine and carboxylic acid. Octadecene is a high boiling temperature organic solvent. Both of oleylamine and carboxylic acid are capping agents. In this synthetic procedure, carboxylic acid could react with metal precursors to substitute the original group in the resulting of mass-action [77, 78], and also react with oleylamine generating water. These two simultaneous reactions and the reaction production will affect nucleation and growth of nanocrystals, but the mechanism is as yet unclear.

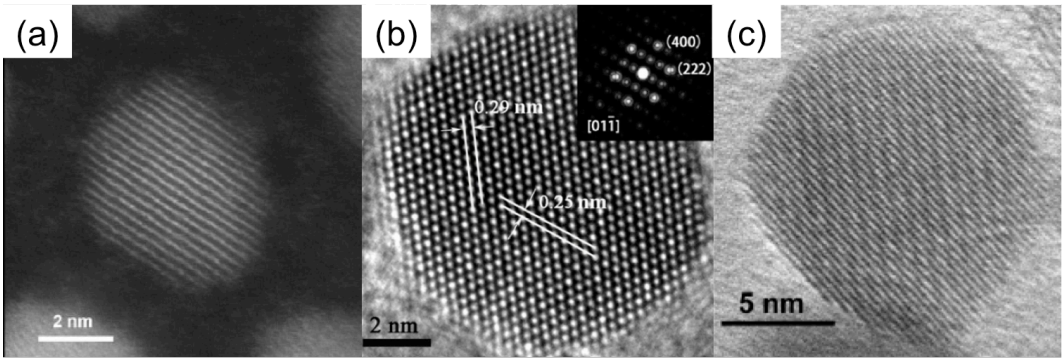

Figure 10. TEM images of ITO NCs synthesized through hot-injection method. (a) reproduced from reference [79]; (b) reproduced from reference [80]; (b) reproduced from reference [81].

The hot-injection method is an improved synthetic approach having similar mechanism with one-pot method, but the substitution reaction and condensation reaction are separated through delaying the time of adding amine. This separation avoids the interaction between the two reactions, and simplifies the mechanism compared with one-pot method. In the one-pot approach, the hydrolysis reaction not only happened between water and metal precursors, but also happened between water and metal-carboxylate that is created through the reaction between precursors and carboxylic acid. Alternatively, the hydrolysis reaction only happened between water and metal-carboxylate in the hot-injection method. We believe the simple reaction path way would be better to form the spherical ITO NPs (*figure 10*). In this reaction process indium and tin precursors react with carboxylic acid (myristic acid) [79] and 2-ethylhexnoic acid [80] in octadecene to

generate metal-carboxylate. Subsequently, oleylamine is injected at high temperature. Water is created through the condensation reaction between amine and carboxylic acid. Simultaneously, the growth of NPs starts through the hydrolysis reaction between metal-carboxylate and water. In another hot-injection recipe [81], the sequences of carboxylic acid and amine are switched. Although the mechanism is unclear, it could still produce good quality spherical ITO NPs (*figure 10c*).

2. Experiments

2.1 Materials

Indium(III) acetate ($In(Ac)_3$, 99.99%) was purchased from Alfa Aesar. Tin(II) 2-ethylhexanoate (95%), copper acetate ($Cu(Ac)_2$, 98%), benzene-1,3,5-tricarboxylic acid (BTC, 95%), acetic acid glacial (>99.85%), oleylamine (OLA, >70%), 1-octadecene (ODE, 90%), 2-ethylhexanoic acid (99%) and (3-Aminopropyl) triethoxysilane (99%) were bought from Sigma-Aldrich. Ethyl acetate (99.9%) from Fisher Scientific, n-hexane (95%) from J.T. Baker, anhydrous tetrachloroethylene (TCE, 99%) from Cole-Parmer, ACS grade of ethanol (>99.5%) from Macron chemicals were used for rinsing solvents. All chemicals were used as purchased without further purification. Glass slide with 1.0 mm thickness as substrates were purchased from VWR International.

2.2 Characterizations

X-ray diffraction (XRD) patterns were obtained using a Bruker-AXS D8 Discover x-ray diffraction instrument, operating at 40 kV and 40 mA with Cu Kα radiation (0.154 nm) with an increment of 0.05. Scanning electron microscope

(SEM) images were formatted by an FEI Quanta 600 using 10 kV accelerating voltage. A thin gold/palladium layer was coated on the samples to increase electrical conductivity. Capping agents and gas sensing properties were measured through a Thermo Scientific Nicolet 6700 Fourier transform infrared (FT-IR) spectrometer. Plasmonic effect was characterized with JASCO V-670 UV-VIS-NIR spectrometer. FEI Titan 80-300 was used for high-resolution transmission electron microscopy (HRTEM) images at 300 kV.

2.3 Tin-doped indium oxide nanocrystals (ITO NCs) synthesis

A hot-injection method was employed to synthesize colloidal ITO NCs. Solution A containing $In(Ac)_3$ (1.08 mmol), Tin(II) 2-ethylhexanoate (0.12 mmol), 2-ethylhexanoic acid (3.6 mmol), and octadecene (10 mL) was loaded in a three-neck flask and stirred under vacuum at 80°C for 30 min; and purged with Ar gas and stirred for 60 min at 150°C. Simultaneously, Solution B including oleylamine (10 mmol) and octadecene (5 mL) in a small vial was stirred at 100°C for 60 min were purged with Ar gas. Solution B was injected to the three-neck flask when the temperature of solution A was increased to 240°C. This reaction solution was held at 290°C for 2 hrs. Then cool down to room temperature, 60 mL of ethyl acetate was added, following by centrifuging at 6000 rpm for 10 min to precipitate the ITO NCs. Supernatant was not needed. Precipitation was re-dispersed in 5 mL

toluene and 10 mL of ethyl acetate were added to agglomerate ITO NCs followed by centrifuging at 6000 rpm for 2 min. Supernatant was discarded, and the final product was re-dispersed in 8 mL toluene for later use. The ITO NCs for UV-VIS-NIR spectrum characterization was prepared from 1 mL of the ITO/toluene solution adding 2 mL ethyl acetate followed by centrifuging at 6000 rpm for 5 min, and repeating this washing step another two times. The final product was re-dispersed in 1 mL tetrachloroethylene.

2.4 Surface modification of ITO NCs

In the surface modification reaction, 2 mL of fresh-synthesized ITO NCs solution (all the synthesized ITO NCs were dispersed in 8 mL toluene), 1 mL toluene, 50μL (0.022 mmol) (3-Aminopropyl)triethoxysilane (APTES), 1 mL acetic acid/toluene solution (contains 2 μL glacial acetic acid, 0.035 mmol) were loaded in a vial and magnetic stirred at room temperature for 30 min followed by centrifuging at 6000 rpm for 5 min. Supernatant was discarded and 5 mL toluene added to wash the precipitated NCs with shaking. This centrifugation and washing was repeated 3 times. The last time washing solvent was 5 mL ethanol to remove remaining toluene through shaking and centrifuging at 6000 rpm for 10 min. The final product – surface modified ITO (APTES-ITO) was dispersed in 1 mL D.I. water.

2.5 APTES-ITO NP thin films

APTES-ITO thin films were fabricated by spin-coating method. Glass slide was sequentially rinsed by acetone, methanol and D.I. water for cleaning. 50 μL of the surface modified ITO NCs (APTES-ITO) dispersed in water were spin-coated on a glass substrate (~1.5 cm x ~1.5 cm) at 2500 rpm for 60s.

2.6 Cu-BTC films

The Cu-BTC thin films were grown on APTES-ITO coated glass substrate using stepwise layer-by-layer (LBL) method. In the typical procedure, the APTES-ITO NP coated glass substrate was immersed in the metal precursor solution containing 1 mmol of $Cu(Ac)_2$ and 30 mL ethanol for 20 min. Successfully, immersed the APTES-ITO coated glass substrate in the organic ligand solution including 0.1 mmol of BTC and 30 mL ethanol for 40 min. Between each step, substrate was rinsed with ethanol to remove unreacted compounds followed by drying in N_2 gas flow at room temperature. This step is needed to fabricate uniform MOF thin film.

2.7 Gas sensing measurement

The flow gas-cell for NIR absorption (*figure 11*) was designed as a cannulate rubber with two closing ends. The light inside end is covered by glass with

sandwich ITO/MOF. The other end is covered by sapphire. After purging the gas-cell with ultra-high purity Ar gas for 1 hour at room temperature, base line was established. Subsequently, another gas flow containing 1% CO_2 in N_2 was passed through the flow-cell at atmospheric pressure with a flow rate of 5 mL min^{-1} using mass-flow-controllers.

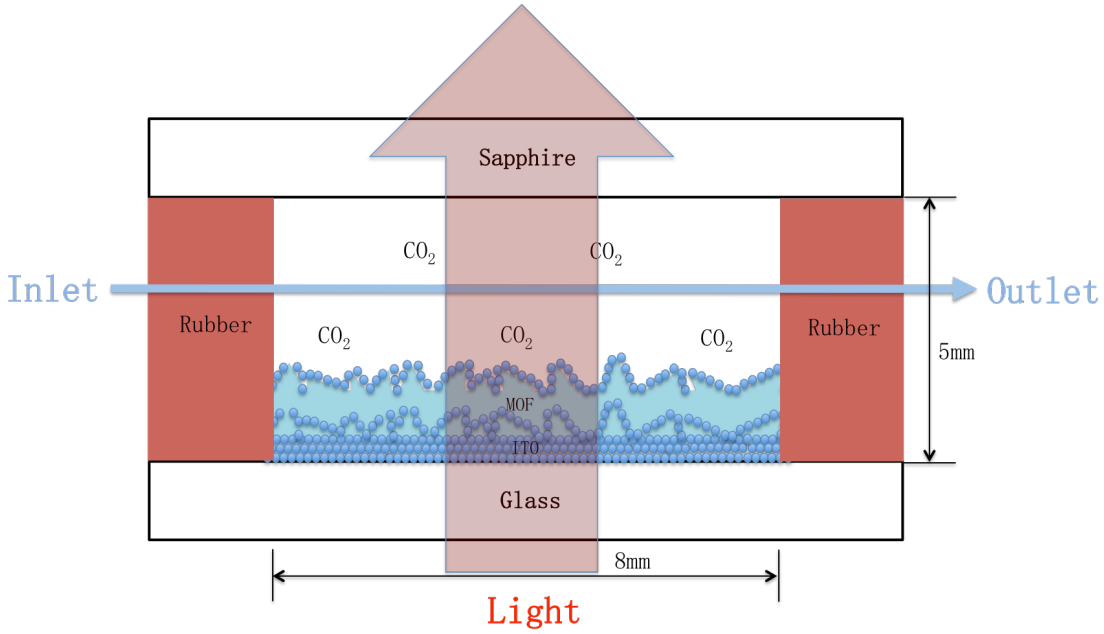

Figure 11. Schematic diagram of flow-cell with a dimension of 8mm x 8mm x 5mm.

3. Results and Discussions

3.1 Characterization of as-synthesized ITO NCs

ITO NCs were synthesized by hot-injection method [80]. Here we selected 10% Sn-doped ITO NCs, because the prior studies showed that 10% Sn doping provided the strongest plasma absorption due to the highest free electron density [76,80,82]. At a lower level of Sn doping (<10%), the density of free electron increases with the increment of Sn percentage. Whereas, the density of free electron decreases with the increment of Sn percentage higher than 10%, caused by the distortion of Indium oxide crystal lattice. Transmission electron microscopy (TEM) imaging (*figure 12*) shows that ITO NCs were spherical shape and not agglomerated due to the segregation by surface capping agent on each NCs. The high-resolution TEM (HRTEM) exhibits that ITO NCs are highly crystalline with an atomic lattice fringe of 0.29 nm corresponding to interplanar spacing of (222) and 0.25 nm for (400) lattice planes.

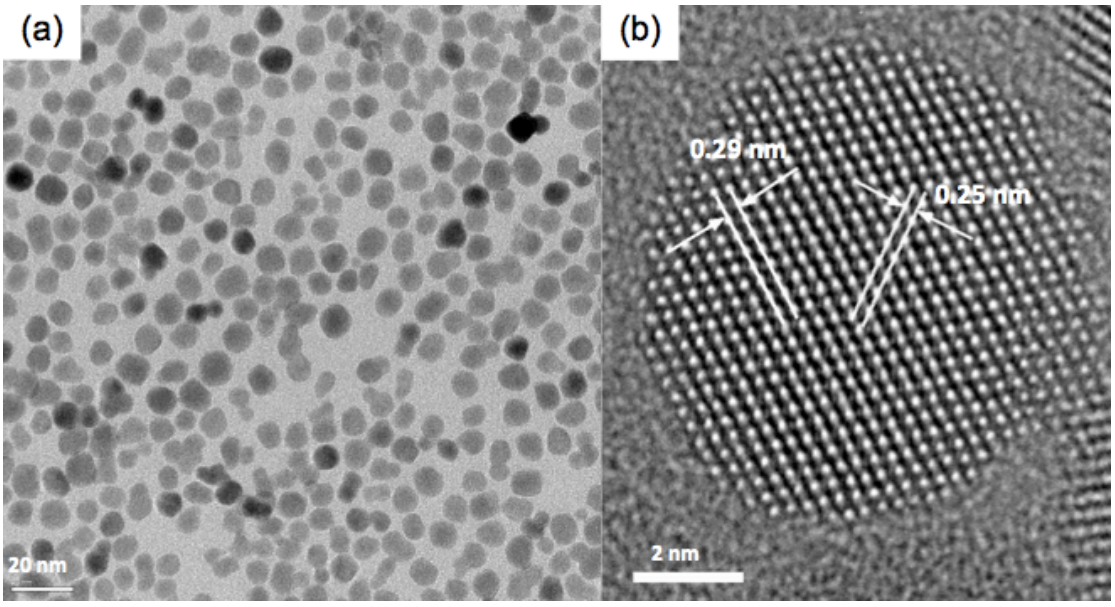

Figure 12. ITO NCs (10% Sn precursor) from the hot-injection method (a) a typical TEM image; (b) a typical HRTEM image.

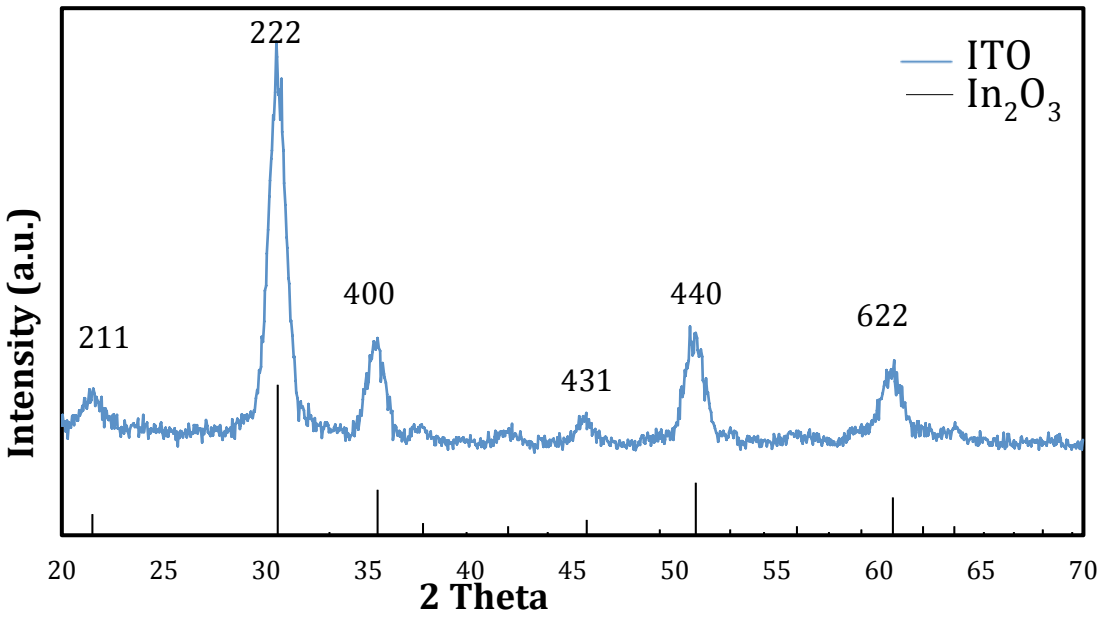

Figure 13. XRD spectrum of ITO nanoparticles (blue line) and corundum-In_2O_3 (vertical lines is JCPDS pattern of In_2O_3 with the pattern number: 06-0416).

The XRD pattern of 10%-Sn ITO (*figure 13*) clearly shows that all the main peaks of synthesized ITO NCs match well with th diffraction peaks of corundum-type indiun

oxide (JCPDS file No. 06-0416). Based on the XRD patterns, the estimated average crystal size could be calculated using Debye-Scherrer equation:

$$D = \frac{k\lambda}{\beta cos\theta} \quad (3)$$

where D is the crystal size in nanometers, λ is the wavelength of X-ray in nanometers (for Cu Kα radiation, $\lambda = 0.154$), β is the calibrated full width at half maximum (FWHM) of the XRD peaks in radians, θ is the Bragg diffraction angle, and for the spherical crystals without cubic symmetry $k = 0.89$. According to the FWHM of the four most intense peaks [(222), (400), (440), and (622)] (*table 1*), the calculated average crystal diameter of ITO NCs is 12 nm [83,84]. Although this average size is not precise enough, if only consider the crystal size; an error of few nanometers may exist because of both crystal size and size distribution will affect the FWHM in XRD pattern. But this calculated average crystal size still shows ITO NCs have small sizes.

Table 1. XRD data for ITO NCs

Peak	2θ (deg.)	FWHM (rad.)	D (nm)	Ave. D (nm)
(222)	30.536	0.0150	9.465	12.041
(400)	35.305	0.0139	10.340	
(440)	50.869	0.0131	11.610	
(622)	60.588	0.00948	16.749	

3.2 Cu-BTC MOF grow on ITO NCs coated glass

Initially, we directly deposited freshly prepared 10% Sn-doped ITO NCs onto a glass substrate by spin coating from TCE and then grow Cu-BTC MOF using the LBL method. Due to the surface capping (Oleylamine and carboxylic acid) on the outside of ITO NCs, the Cu-BTC MOF couldn't grow on this ITO layer. In order to grow the Cu-BTC MOF, two methods were attempted to remove the surface ligands from ITO NCs. The first procedure is using O_2 plasma to treat the ITO coating layer on glass substrate. The bombardment of high energy O_2 plasma could remove all the residual organic compounds and produce hydroxyl groups on the surface which provide terminated groups for MOF growing via the stepwise LBL method [9].

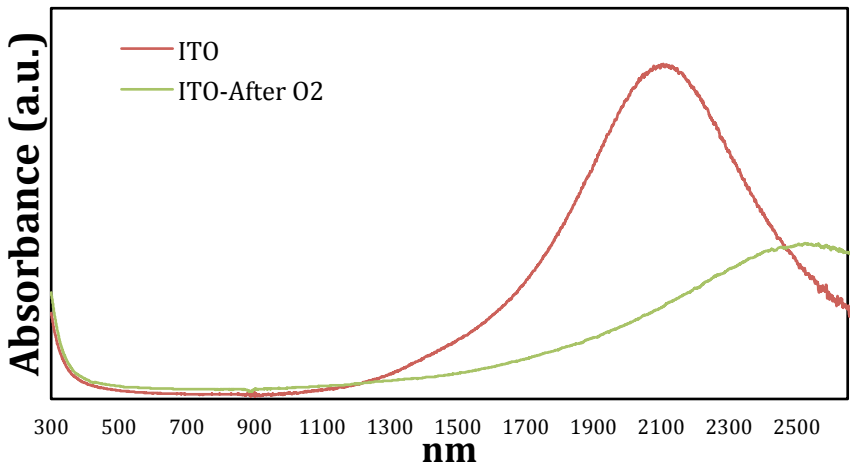

Figure 14. UV-Vis-NIR spectra of the 10% Sn-doped ITO NCs deposited on glass substrate by spin-coating (red line) and ITO film on glass after O_2 plasma treatment (green line).

However, a shift of the LSPR peak after O_2 plasma treatment is observed (*figure 14*) attributed to a decrease of free carrier concentration caused by oxidation of O_2 plasma [9]. O_2 plasma is inapplicable for the second ITO layer on MOF because the high-energy O_2 plasma will also destroy the MOF film. Another method to remove the capping agents from ITO NCs is washing. By repeating a procedure of deposition and dispersion that is flocculating ITO NCs from toluene solvent by adding ethyl acetate and centrifuging, and then re-dispersing precipitated ITO NCs in toluene, part of the capping agents are removed because the ITO NCs could still be dispersed in nonpolar solvent, but ITO NCs flocculate and precipitate on the bottom after few days. The 4-time-washing ITO NCs (mono dispersed in TCE) is deposited on glass substrate using spin coating. Due to insufficient capping agents on the surface, agglomeration of ITO NCs is observed (*figure 15a,b*). By stripping part of the long-carbon-chain capping agents, MOF could grow on the ITO layers. Because hydroxyl groups (-OH) always exist on the surface of metal oxide including ITO NCs. [85]

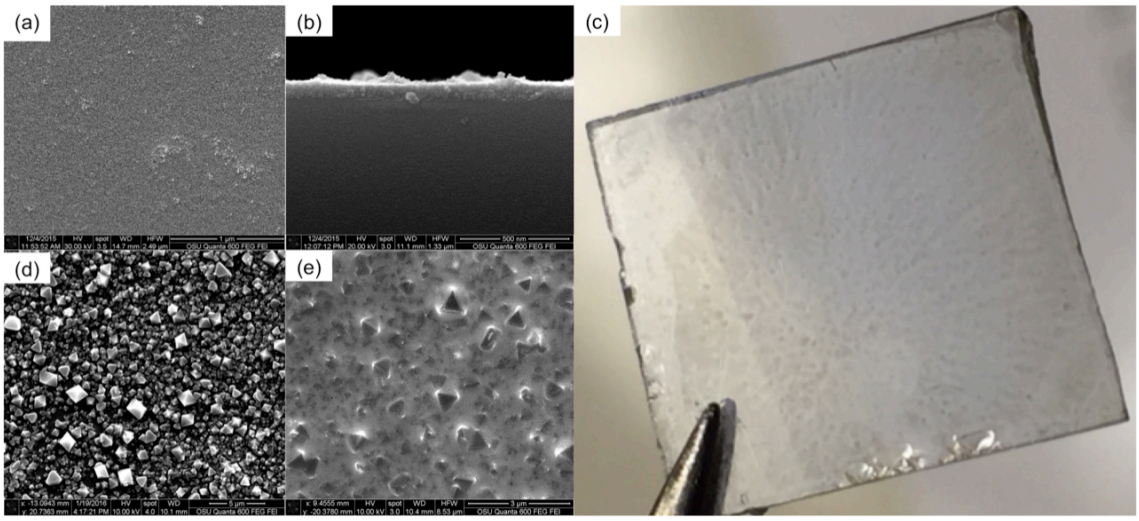

Figure 15. SEM images of the 10% Sn-doped ITO NCs after 4 times washing and residpersed in TCE, then deposited on glass substrate by spin-coating; (a) top view and (b) cross section. (c) is picture for glass/ITO/40MOF/ITO. (d) is SEM images of glass/ITO/40MOF. And (e) is SEM images of glass/ITO/40MOF/ITO.

The growth of MOF on ITO was characterized by XRD pattern and UV-Vis-NIR spectra. In the XRD pattern (*figure 16*), along with the increasing of LBL cycles the intensity of XRD peaks increase indicating the growth of Cu-BTC MOF crystals and film thickness. Polycrystalline structure of Cu-BTC MOF ([111], [200], [220]) is proved by the XRD pattern. Among these peaks, the peak of [222] direction in the XRD pattern is the most intense indicating that [222] is the main orientation of Cu-BTC growing on ITO coated glass substrate through LBL method. The growth of Cu-BTC MOF thin film is also confirmed by the increasing intensity of absorption peak around 700 nm (absorption band) in the UV-Vis-NIR spectra (*figure 17*). LSPR peak shifts to longer wavelength with more LBL cycles (*figure 17 inset*) caused by continuously increasing of MOF crystals size and number.

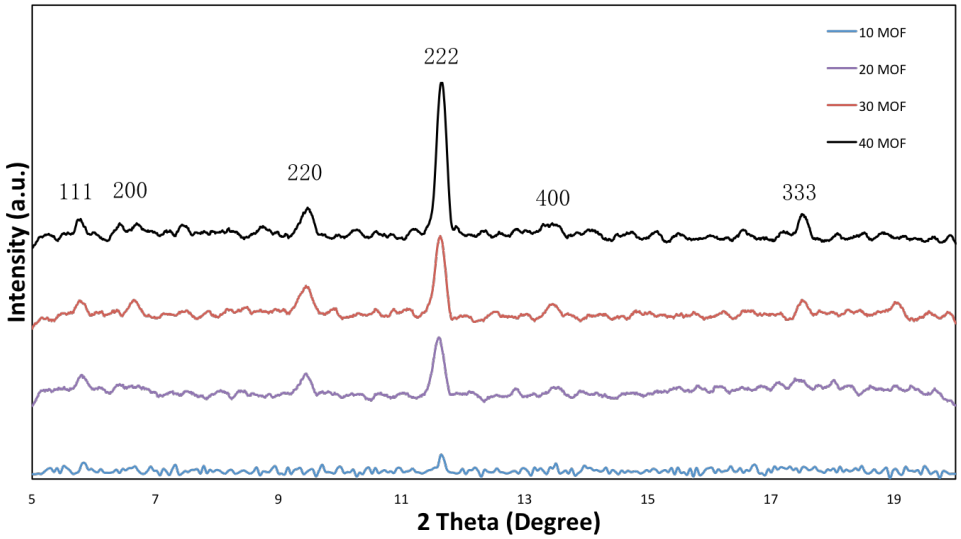

Figure 16. XRD pattern for MOF grow on ITO on glass sbustrate with 10, 20, 30 and 40 LBL cycles.

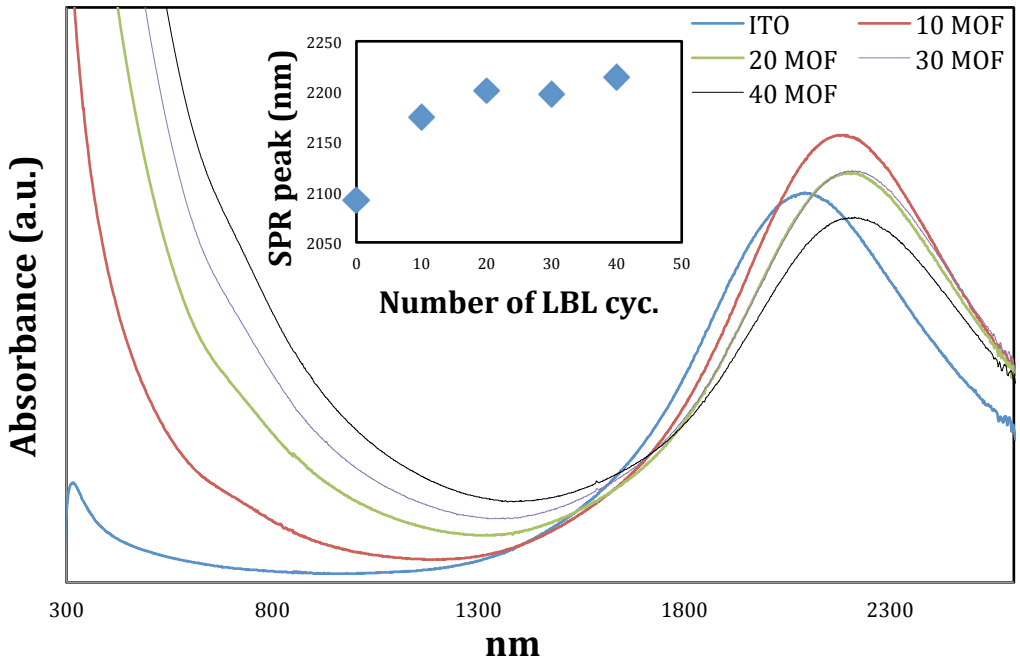

Figure 17. UV-Vis-NIR spectra of Cu-BTC MOF grow on ITO coated glass with 10, 20, 30 and 40 LBL cycles (inset shows location of LSPR peaks with 0,10, 20, 30 and 40 LBL cycles)

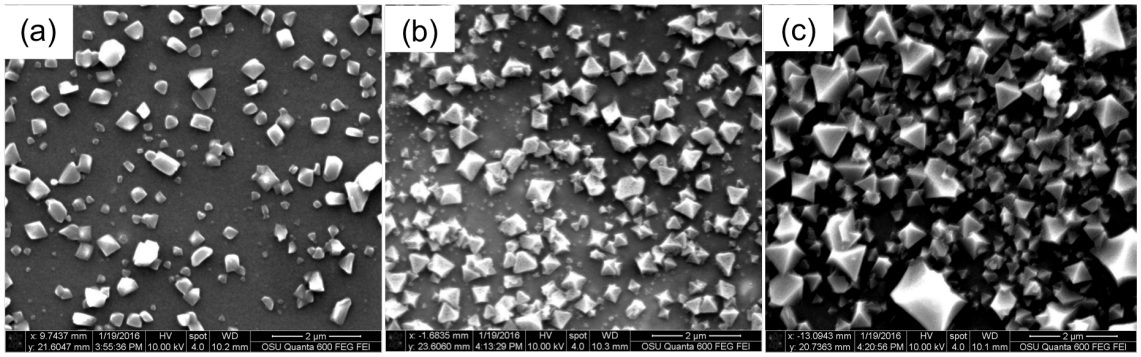

Figure 18. SEM images of Cu-BTC MOF grow on ITO coated glass with (a) 10 LBL cycles, (b) 20 LBL cycles and (c) 40 LBL cycles.

Along with increasing LBL cycles, more new and small MOF crystals grow on the surface and the earlier formed crystals grow bigger (*figure 18*). Simultaneously, MOF thickness and surface coverage increase resulting in change of refractive index (RI) of the MOF layer. The relationship between L peak shift, change of RI and thickness can be described by following equation [22, 86],

$$\Delta\lambda = m(\eta_a - \eta_s)[1 - \exp(-2d/l_d)] \quad (4)$$

Here $\Delta\lambda$ is shift of LSPR extinction wavelength maximum; m is sensitive factor of the sensor related with the bulk reactive-index of the NPs; η_a is refractive index of absorbate layer; η_s is refractive index of surrounding environment on top of the sensing film; d is thickness of adsorbate layer; l_d is electromagnetic-field-decay length. In our case, m is constant and related with RI of ITO layer; l_d is related with incident light. Because we analyze the LSPR peak shift, the incident light wavelength is as same as LSPR wavelength. l_d relates with

LSPR wavelength, based on the modulation of the previous work [9], the decay length is only few nanometer in free space. As the inset of *figure 17* shows, the affection to the decay length from a small change LSPR peak (~100 nm) could be neglected. Correspondingly, the MOF thickness d changes few hundreds nanometers. As a result $1-\exp(-2d/l_d)$ increases direct proportion to MOF thickness. In our experiment, η_a and η_s separately represent the effective RI of Cu-BTC MOF layer (η_a =~1.3 [9] and air (η_s =1). Hence, the shift of LSPR ($\Delta\lambda$) is positive and directly related with increase of MOF thickness (d).

The Cu-BTC MOF film growing on the uneven surface with bulk agglomerated ITO is uniform. After 40 LBL cycles, another layer of ITO is coated on the top of MOF thin film via spin coating of ITO NCs solution. The solution is blocked by the protruding parts and leads to extremely uneven coating of ITO (*figure 15c*). The second ITO layer cover all most the surface of the MOF only top of big MOF crystals exposure outside, lower places are fully covered (*figure 15d,e*). Therefore, the agglomerated ITO NCs of the first ITO layer could not give a smooth surface for a high quality ITO/MOF "sandwich" structure.

3.3 Surface modification of ITO NCs

In order to fabricate better "sandwich" structure, the surfaces of ITO NCs are modified with APTES, which has terminated -NH_2 (*figure 19*). When APTES and

acetic acid are added in ITO/toluene solution, a fast hydroxylation reaction starts between APTES and acetic acid (*figure 20a*) creating hydroxyl group bonding with silicon atom and the by-product ethyl acetate [87]. Further, a condensation reaction (*figure 20b*) happens between hydroxylated APTES and the hydroxyl groups on the surface of ITO NCs producing water [85, 88-90]. Water will also react with APTES yielding hydroxylated APTES (*figure 20c*). Finally, APTES will be anchored on the surface of ITO NCs completely transfer solubility of ITO NCs from hydrophobic to hydrophilic.

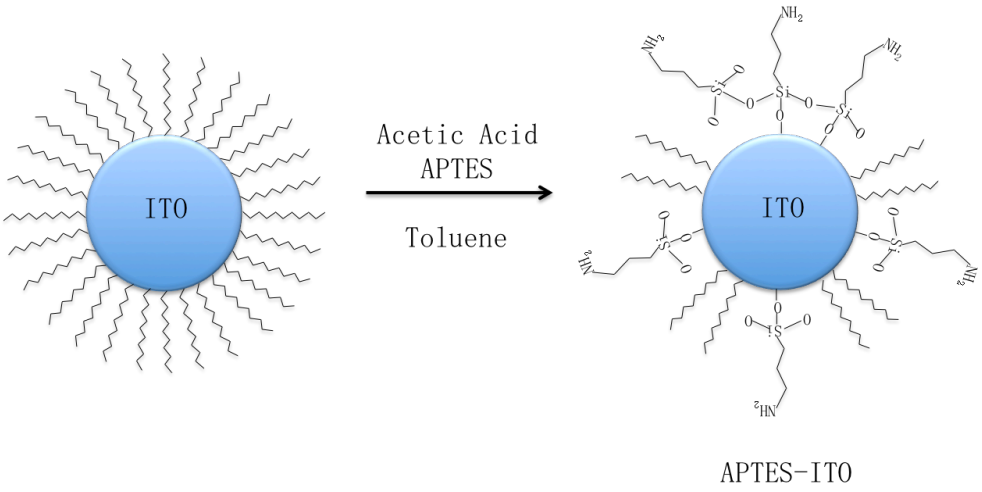

Figure 19. Schematic illustration of ITO NCs surface modification.

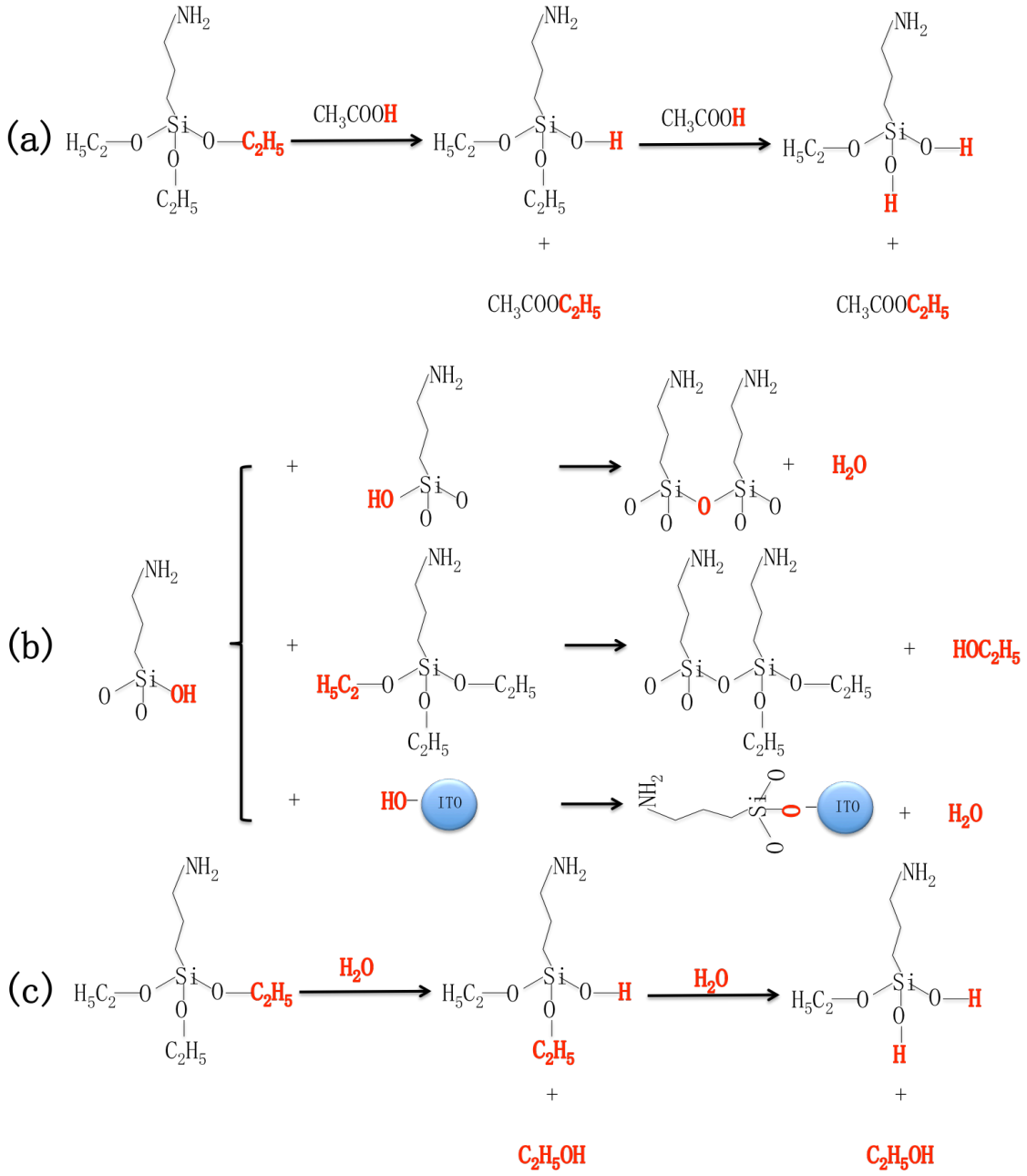

Figure 20. Schematic illustration of ITO NCs surface modification; (1) APTES react with acetic acid; (2) Condensation reaction between hydroxlys; (3) APTES react with water.

The ligand exchange onto ITO NCs is inspected using FI-IR (*figure 21*).

Table 2 gives an overview of the most important IR vibrations before and after surface modification of ITO NCs via APTES ligand exchange. The unmodified ITO

NCs show clear CH_2 peaks at 2926, 2855 and 1466 cm^{-1} and a CH_3 peak at 2956 cm^{-1}. These bands are known as CH_2 chains of oleylamine and 2-ethylhexanoic acid.

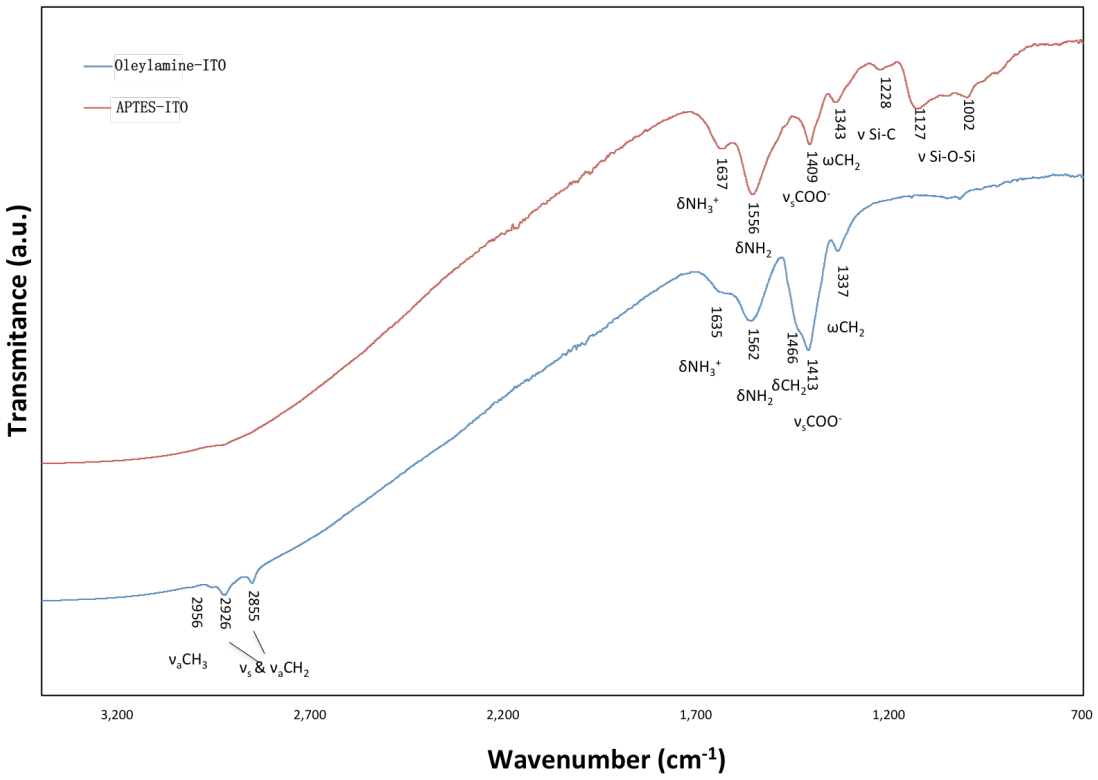

Figure 21. FT-IR sprctra of as-synthesized ITO NCs (blue) and APTES modifided ITO NCs (APTES-ITO, red).

The present of amine and carboxylate are further confirmed by scissoring of amino group at 1562 and 1635 cm^{-1} and symmetric stretching of COO^- at 1413 cm^{-1}. The asymmetric stretching of carboxylate is usually located at around 1500 cm^{-1} [97]. It may overlap with the scissoring absorption peak of amino group and couldn't be clear seen. After surface modification, several new bands are observed in the FT-IR

spectra for APTES-modified ITO NCs (APTES-ITO).

Table 2. Vibrational Modes Observed in FTIR Spectra of OLAM-ITO and APTES-ITO NCs shown in figure21.

wavenumber (cm^{-1})	vibrational modes	reference (cm^{-1})
2956	CH_3 asym stretching	2954 [91]
2926	CH_2 sym stretching	2922 [92]
2855	CH_2 asym stretching	2854 [92]
1637 & 1635	NH_3^+ scissoring	1636 [93]
1562 & 1556	NH_2 scissoring	1565 [94]
1466	CH_2 scissoring	1464 [95]
1413 &1409	COO^- sym stretching	1407 [89]
1343 & 1337	CH_2 wagging	1337 [95]
1228	Si-C	~1200 [96]
1127 &1002	Si-O-Si	1130-1000 [96]

The most striking difference is the appearance of bands between 1000 and 1150 cm^{-1}. These bands are characteristic of Si-O-Si vibrations. Additionally, the peak at 1228 cm^{-1} shows the vibration of Si-C. The exchange of the surface ligand is also confirmed by the disappearance of the alkane chain bands at 2956, 2926, 2855 and 1466 cm^{-1}, because the original surface ligands contain a large number of CH_2 and CH_3. Compared the band intensity of amino group and carboxylate before and after ligand exchange, the amount of carboxylate has a huge decrease after ligand exchange indicating exchange of the surface ligands, but not completely remove the original capping agents.

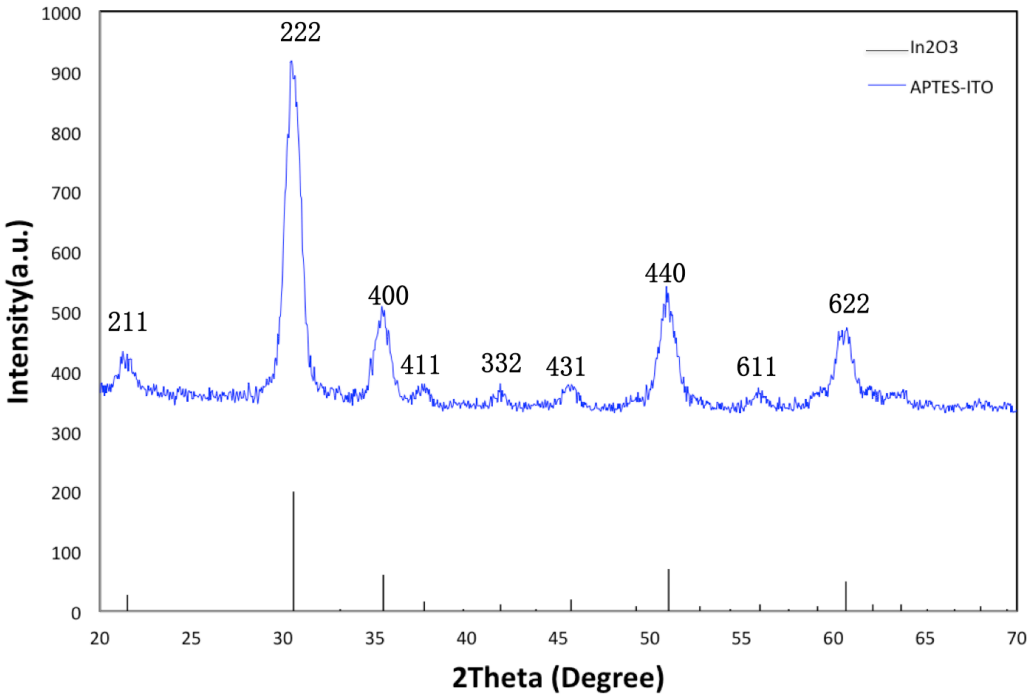

Figure 22. XRD spectrum of APTES-ITO nanoparticles (blue line) and corundum-In_2O_3 (vertical lines; JCPDS:06-0416).

XRD pattern of APTES-ITO (*figure 22*) shows that all the main peaks of surface-modified ITO NCs match well with the diffraction peaks of corundum-type indium oxide (JCPDS file No.06-0416) indicating that the reaction of surface modification doesn't affect the crystal sturcture of ITO NCs.

3.4 CU-BTC MOF grow on APTES-ITO coated glass and sandwich structure of MOF and APTES-ITO

Compared with the film from as-synthesized ITO NCs (*figure 15a,b*), the APTES-ITO film on glass substrate (*figure 23a,b*) is much more uniform because

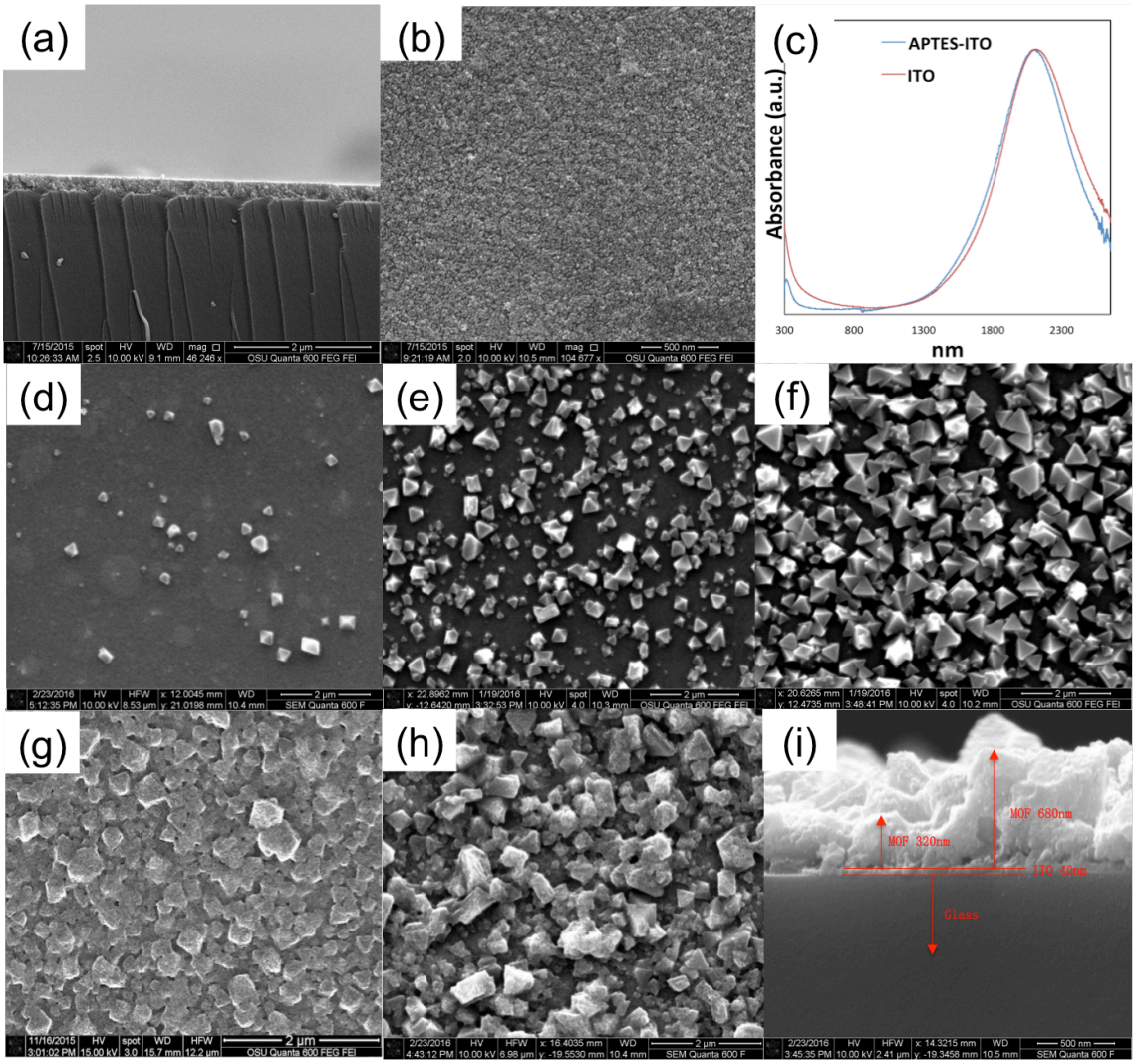

Figure 23. (a) and (b) are SEM images of APTES-ITO NCs coated on glass substrate; (c) is the UV-Vis-NIR spectrum of APTES-ITO (blue) and ITO (red) NCs coated on glass substrate. SEM images of Cu-BTC MOF grow on APTES-ITO coated glass with (d) 10 LBL cycles, (e) 20 LBL cycles, (f) 40 LBL cycles, (h) spin coating another APTES-ITO on the top of 40 LBL cycles MOF (40MOF/AITO), (h) sandwich structure of APTES-ITO and MOF (40MOF/AITO/40MOF/AITO) and (i) sectional view of sandwich the structure (40MOF/AITO/40MOF/AITO).

the new surface ligand prevent the agglomeration between ITO NCs. The LSPR absorption peak (*figure 23c*) of this close packing APTES-ITO NCs locates at 2100 nm as same as ITO film. Growth of MOF crystals on APTES-ITO film is very similar to the growth on ITO film. Small Cu-BTC MOF crystals grow on some points on

APTES-ITO film surface. With increasing the LBL cycles, more crystals appear and crystals size keep growing (*figure 23d,e,f*). With further increas of LBL cycles till to 40 LBL cycles, the surface is almost fully covered by the Cu-BTC MOF (figure 23f). Then the second APTES-ITO layer is coated on the 40 LBL cycles Cu-BTC MOF (*figure 23g*). Sequentially, another 40 LBL cycles Cu-BTC MOF is grown and followed with the third APTES-ITO coating (*figure 23h,i*). In this sandwich sturcture, the first APTES-ITO layer on glass is about 40 nm (*figure 23i*). The second and third APTES-ITO layer couldn't be observed from SEM image of the cross section because most of the APTES-ITO NCs accumulate in the valleys between Cu-BTC MOF crystals and a small quantity of these NCs absorb on surface of MOF crystals. Due to the coverage of APTES-ITO NCs, the MOF crystal size could not be separately examined, the variety of their crystal sizes is clearly observed (*figure 23g,h,i*). The crystal size could grow as big as 680 nm after the second 40 LBL cycles growing procedure.

With increase of LBL growth cycles, the diffraction peaks (*figure 24*)more clearly reveal the presence of polycrystalline structure. Although, the mechanism of Cu-BTC MOF growing on metal oxide capped wiith -NH_2 terminated ligand has not been fully comprehended, the presence of –NH_2 functional groups at the end of APTES would induce the growth of Cu-BTC MOF, but lead to unoriented growth (*figure 24*).

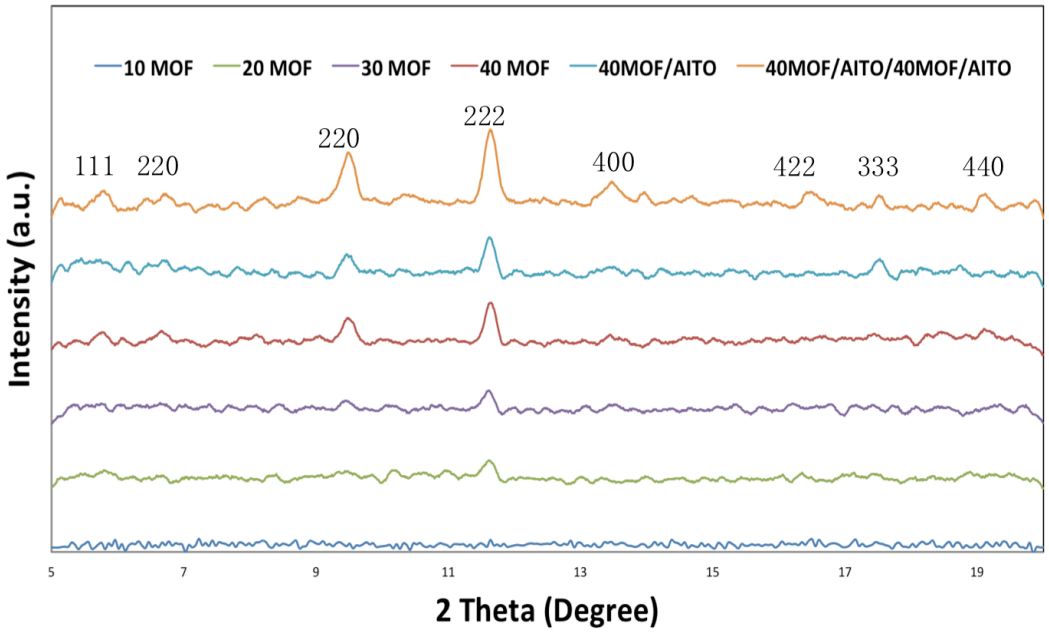

Figure 24. XRD spectrum of MOF growing on APTES-ITO coated glass and MOF/AITO/MOF/AITO sandwich structure.

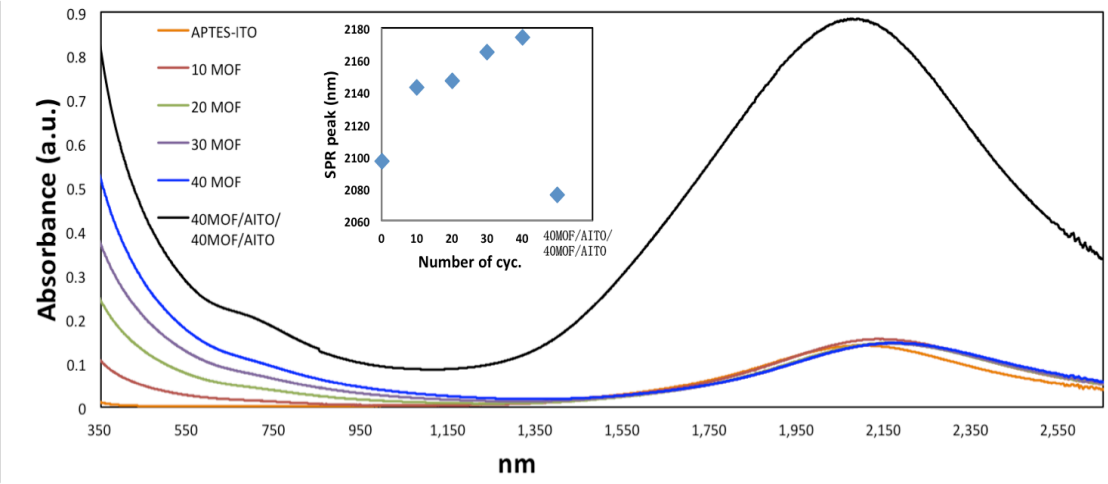

Figure 25. UV-Vis-NIR spectra of Cu-BTC MOF grow on APTES-ITO coated glass with 10, 20, 30, 40 LBL cycles and and MOF/AITO/MOF/AITO sandwich sturcture (inset shows location of LSPR peaks with 0, 10, 20, 30, 40 LBL cycles and MOF/AITO/MOF/AITO sandwich sturcture).

The UV-Vis-NIR absorption spectra (*figure 25*) display how the optical absorption changes after each stage of film deposition and processing. In the case

of Cu-BTC MOF growing on the first APTES-ITO layer coated on glass, owing to the change of refractive index [22,86] on the surface of APTES-ITO layer, the absorption peak shift to longer wavelength with the growth of Cu-BTC MOF (*figure 25 inset*). The trend of the LSPR peak moving could also be explained by *equation (4)*. But the absorption peak of the sandwich structure (MOF/AITO/MOF/AITO) shifts back to a shorter wavelength and even shorter than the absorption peak of APTES-ITO coated on glass, because the LSPR is sensitive to changes in the local dielectric environment [98-100]. Research [98] has shown the plasmon wavelength of truncated tetrahedra silver particles was linearly dependent on refraction index of substrate and indicated high external dielectric constant lead to big shift of plasmon resonance wavelength to longer range. Similarly, the first APTES-ITO coated on glass has a higher RI (~1.5) than the RI (~1.3) of the second and third APTES-ITO that are coated on Cu-BTC MOF. Additionally, ascribing to the rough surface of Cu-BTC MOF, the second and third layers contain more of APTES-ITO NCs than the first layer. The UV-Vis-NIR absorption spectra (*figure 25*) reveals a huge increase of aborptance at ~2100 nm for the sandwich srtucture indicating the different amount of APTES-ITO NCs between the first layer and other two layers. Hence, the LSPR wavelength of the sandwich structure is dominated by the second and third ITO layer growth on Cu-BTC MOF layer, and leads to a shorter LSPR wavelength.

3.5 Sensing capabilities

To detect the performance of the fabricated NIR absorption sensor, a gas-flow cell is designed (*figure 11*). For the measurement of transmittance (T%), the FT-IR chamber is previously filled with pure N_2 to prevent the diffusion of atmospheric CO_2. Before flowing the 1% CO_2 in N_2, ultra-high purity Ar gas is purged in the flow cell for 1 hr. FT-IR absorption spectra of CO_2 are measured for the sensing performance of different functional layers shown in *figure 26*.

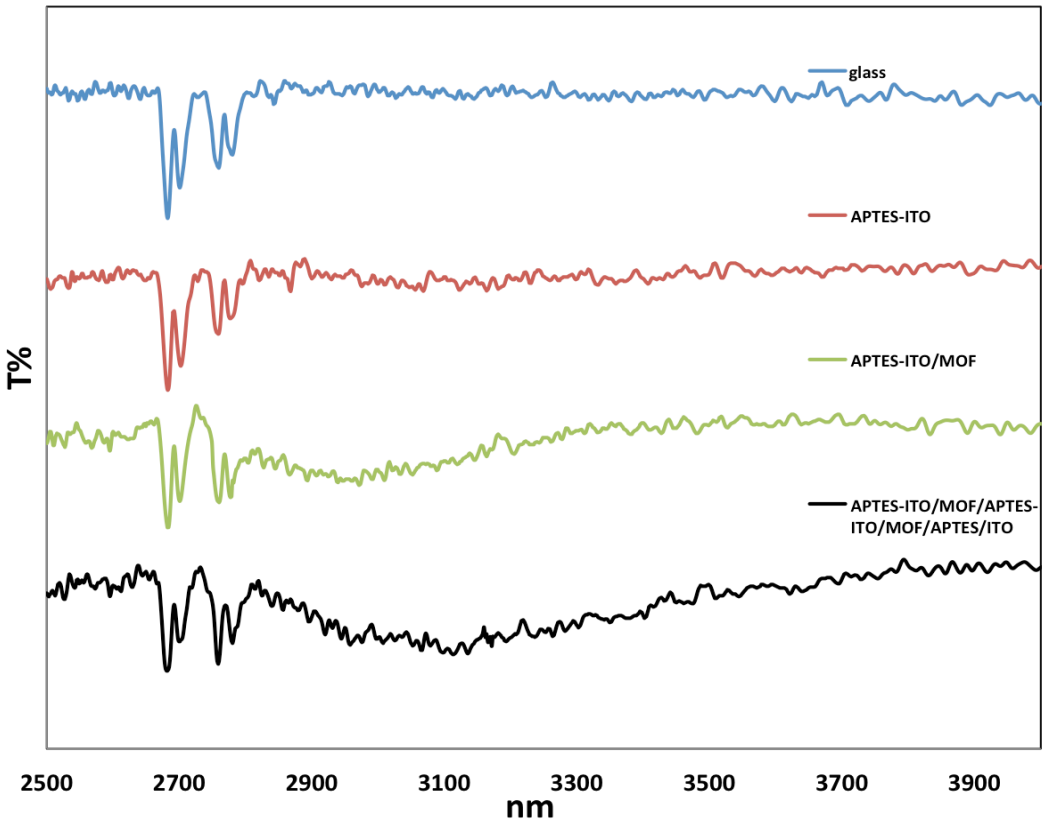

Figure 26. FT-IR spectra of 1% concentration of CO_2 flowing on bare glass (blue line), APTES modified 10% Sn-doped In_2O_3 coated on glass (red line), 40 LBL cycles MOF growing on APTES-ITO coated glass (green line) and sandwich structure of 3 APTES-ITO layers and two 40-LBL-cycles MOF layers (black line).

The bare glass is first investigated. Sequentially, APTES modified 10% Sn-doped In_2O_3 coated on the glass is measured. Compared with bare glass, no distinct different are found for the CO_2 absorption peaks in the range from 2600 nm to 2800 nm. Same results are observed from the investigation of 40 LBL cycles MOF growing on APTES-ITO (10% Sn) coated glass and the sandwich-structured film containing 2 layers of 40-LBL-cycles MOF and 3 layers of APTES-ITO (10% Sn). In addition, a broad absorption peak (around 3100 nm) of water is found in both of the FT-IR spectra. Although it is not clear where the water comes from, water is a possible cause for the malfunction of this MOF/ITO film in CO_2 sensing application. Research [101,102] showed that Cu-BTC has a very large capacity for water in preference to CO_2. Therefore, the presence of water will significantly decrease the adsorption of CO_2, because water competitively adsorbs in the pores of Cu-BTC MOF, blocking access for CO_2.

4. Conclusion and future work

The surface of ITO NCs was successfully modified by APTES, which provided –NH_2 terminated functional group that transforms the wettability of the as-synthesized ITO NCs from hydrophobic to hydrophilic. The new surface ligand capped ITO NCs were characterized by HRTEM, XRD, SEM, UV-Vis-NIR and FT-IR to evaluate changes of properties after surface modification. The APTES-ITO was applied to fabricate NIR gas sensors, where Cu-BTC MOF thin film was grown on the modified ITO NC film surface to create a sandwich-structured film of ITO and MOF on glass substrate by repeating coating APTES-ITO and growing Cu-BTC MOF. However, these thin-film sensors did not show enhanced absorption of CO_2 peaks in the NIR range between 2600 nm and 2800 nm.

A possible cause for these non-functional thin film sensors is attributed to the presence of water. The porous Cu-BTC MOF competitively adsorbs water, blocking the access of CO_2. Due to the competitive adsorption of water, the sandwich-structured MOF/ITO film shows no enhancement for the detection of CO_2. In future work, a drying or a water separation membrane will be added to remove water from the gas flow.

In addition to the interference of water, the length of surface ligand could be another factor in the poor performance of the thin film sensor. Although the role of the ligand length to the plasmonic enhancement of ITO NCs is not well understood,

studies about the SAMs' chain length to the sensing capability of Ag nanoparticles [103] and the SiO_2 shell thickness to the sensing capability of Au nanoparticles [104] have been reported. The study of Ag nanoparticles [103] showed that the nanoparticles' sensitivity was attenuated when the nanoparticles were modified with long-chain SAMs and the longest-chain SAMs (~2 nm) weakened the sensitivity by 20%. The study of SiO_2 shelled 55nm Au nanoparticles [104] showed that the enhanced electric field reduced to half when the silica shell thickness increased from 2 nm to 4nm. Further, the enhancement almost approaches to zero with a shell thickness of 20 nm. Regarding the APTES-ITO NCs, long-chain surface ligands were likely generated from the condensation reaction between APTES molecules (*figure 20*) during the surface modification procedure. The long-chain surface ligands could potentially block the analyte entering the enhanced electric filed which is few nanometers around ITO NCs [9]. In addition, MOF grow on APTES-ITO film may be separated from the enhanced electric field of ITO film by the long chain surface ligands existed on APTES-ITO surface. Therefore, signal intensity couldn't be observed without the interaction between enhanced electric field and analyte molecules. In the future, studies onethe length of the surface ligand and its impact on plasmonic effect on ITO NCs need to be carried out.

In addition to the presence of water and surface ligand, the gas cell thickness is another important factor for the poor performance in IR sensing. The gas cell

design needs to be improved in the future. The thickness of the gas cell plays an important role in the signal intensity, because the signal enhancement from absorption of analyte in MOF would be small, if the gas cell has a large thickness. Based on the Beer-Lambert law (*equation 1*), a thicker gas cell gives a longer light path length and will provide a relatively stronger absorption signal of the analyte in the gas phase. Based on the case of Cu-BTC for CO_2 absorption, a simple calculation is given below: For a gas cell with the size $8\,mm \times 8\,mm \times 5\,mm$, the volume is $320\,mm^3$. Neglect the volume decreasing from the MOF layer which has a few hundreds nanometers thickness. Based on the equation $PV = nRT$, assume the pressure is 101 kPa, temperature is $295\,K$, the mount of CO_2 (1% CO_2 in N_2) in the gas cell is

$$n_{CO_2-cell} = \frac{PV}{RT} = \frac{\frac{1}{100} \times 100kPa \times 320\,mm^3 \times 10^{-6}\,\frac{L}{mm^3}}{8.314\,kPa{\cdot}\frac{L}{k} \times 295K} = 1.3{\times}10^{-7}\,mol.$$

The density of Cu-BTC MOF is 0.35 g/cm [the production of Chemicals Company SIGMA-ALDRCH]. Data in a journal paper [105] shown the absorption capacity of CO_2 in Cu-BTC MOF was linear with the pressure in a low-pressure range from 0 to 1000 mbar. At 100 mbar, the capacity of CO_2 is $0.5\,mol/kg$. For a Cu-BTC layer with 100 nanometters thickness and in a gas flow containing 1% CO_2 in N_2 under 100 kPa pressure, the amount of absorbent CO_2 is

$$n_{CO_2-MOF} = m_{MOF} \times \frac{0.01 \times 100\,kPa \times \frac{1\,mbar}{0.1\,kPa}}{100\,mbar} \times 0.5\,\frac{mol}{kg}$$

$$= 8\ mm \times 8\ mm \times 100\ nm \times \frac{0.35g}{cm^3} \times 0.05\ \frac{mol}{kg}$$

$$= 1.12 \times 10^{-10}\ mol$$

The percentage of CO_2 for every 100-nanometer MOF vs. CO2 in the free space of the gas cell is:

$$\frac{n_{CO_2-MOF}}{n_{CO_2-cell}} = 0.089\%$$

For our thin film sensor with an average MOF thickness about 500 nm, the CO2 absorption in MOF is 0.446% compared with the amount of CO2 in the cell out of MOF layer. If the thickness of the cell could be decreased to micrometers' scale, the signal increasing from the MOF layer would be much more considerable.

Bibliography

[1] Shekhah, O., Wang, H., Paradinas, M., Ocal, C., Schüpbach, B., Terfort, A., Zacher, D., Fischer R. A., & Wöll, C. (2009). Controlling interpenetration in metal-organic frameworks by liquid-phase epitaxy. *Nature materials*, *8*(6), 481-484.

[2] Furukawa, H., Cordova, K. E., O'Keeffe, M., & Yaghi, O. M. (2013). The chemistry and applications of metal-organic frameworks. *Science*, *341*(6149), 1230444.

[3] Yaghi, O. M., O'Keeffe, M., Ockwig, N. W., Chae, H. K., Eddaoudi, M., & Kim, J. (2003). Reticular synthesis and the design of new materials. *Nature*, *423*(6941), 705-714.

[4] Li, J. R., Kuppler, R. J., & Zhou, H. C. (2009). Selective gas adsorption and separation in metal–organic frameworks. *Chemical Society Reviews*, *38*(5), 1477-1504.

[5] Férey, G. (2008). Hybrid porous solids: past, present, future. *Chemical Society Reviews*, *37*(1), 191-214.

[6] Li, S. L., & Xu, Q. (2013). Metal–organic frameworks as platforms for clean energy. *Energy & Environmental Science*, *6*(6), 1656-1683.

[7] Kreno, L. E., Leong, K., Farha, O. K., Allendorf, M., Van Duyne, R. P., & Hupp, J. T. (2011). Metal–organic framework materials as chemical sensors. *Chemical Reviews*, *112*(2), 1105-1125.

[8] Lu, G., Farha, O. K., Zhang, W., Huo, F., & Hupp, J. T. (2012). Engineering ZIF-8 Thin Films for Hybrid MOF-Based Devices. *Advanced Materials*, *24*(29), 3970-3974.

[9] Kim, K. J., Chong, X., Kreider, P. B., Ma, G., Ohodnicki, P. R., Baltrus, J. P., Wang, A. X. & Chang, C. H. (2015). Plasmonics-enhanced metal–organic framework nanoporous films for highly sensitive near-infrared absorption. *Journal of Materials Chemistry C*, *3*(12), 2763-2767.

[10] Lu, Z. Z., Zhang, R., Li, Y. Z., Guo, Z. J., & Zheng, H. G. (2011). Solvatochromic behavior of a nanotubular metal– organic framework for sensing small molecules. *Journal of the American Chemical Society*, *133*(12), 4172-4174.

[11] Lai, W. C., Chakravarty, S., Wang, X., Lin, C., & Chen, R. T. (2011). On-chip methane sensing by near-IR absorption signatures in a photonic crystal slot waveguide. *Optics letters*, *36*(6), 984-986

[12] Robinson, J. T., Chen, L., & Lipson, M. (2008). On-chip gas detection in silicon optical microcavities. *Optics Express*, *16*(6), 4296-4301.

[13] Hasan, D., & Wang, A. X. (2013, February). Enhanced localized surface plasmonic resonance in dielectric photonic band gap structures: Fabry-Perot nanocavity and photonic crystal slot waveguides. In *SPIE OPTO* (pp. 863203-863203). International Society for Optics and Photonics.

[14] Crawford, M. F., & Dagg, I. R. (1953). Infrared absorption induced by static electric fields. *Physical Review*, *91*(6), 1569.

[15] Terhune, R. W., & Peters, C. W. (1959). Electric field induced vibration rotation spectrum of H 2 and D 2. *Journal of Molecular Spectroscopy*, *3*(1), 138-147.

[16] Callaway, J. (1964). Optical absorption in an electric field. *Physical Review*, *134*(4A), A998.

[17] Ahn, D., & Chuang, S. L. (1987). Intersubband optical absorption in a quantum well with an applied electric field. *Physical Review B*, *35*(8), 4149.

[18] Anastassakis, E., & Burstein, E. (1970). Electric-field-induced infrared absorption and Raman scattering in diamond. *Physical Review B*, *2*(6), 1952.

[19] Courtois, D., & Jouve, P. (1975). Electric field induced infrared spectrum of nitrogen: Vibrational polarizability matrix elements. *Journal of Molecular Spectroscopy*, *55*(1-3), 18-27.

[20] Comin, A., & Manna, L. (2014). New materials for tunable plasmonic colloidal nanocrystals. *Chemical Society Reviews*, *43*(11), 3957-3975.

[21] Mayer, K. M., & Hafner, J. H. (2011). Localized surface plasmon resonance sensors. *Chemical reviews*, *111*(6), 3828-3857.

[22] Willets, K. A., & Van Duyne, R. P. (2007). Localized surface plasmon resonance spectroscopy and sensing. *Annu. Rev. Phys. Chem.*, *58*, 267-297.

[23] Hutter, E., & Fendler, J. H. (2004). Exploitation of localized surface plasmon resonance. *Advanced Materials*, *16*(19), 1685-1706.

[24] Farvid, S. S., Dave, N., Wang, T., & Radovanovic, P. V. (2009). Dopant-induced manipulation of the growth and structural metastability of colloidal indium oxide nanocrystals. *The Journal of Physical Chemistry C*, *113*(36), 15928-15933.

[25] Martinez, M. A., Herrero, J., & Gutierrez, M. T. (1995). Thin Solid Films, 269(1), 80-84.

[26] Noh, J. H., Han, H. S., Lee, S., Kim, J. Y., Hong, K. S., Han, G. S., Shin, H. & Jung, H. S. (2011). Advanced Energy Materials, 1(5), 829-835.

[27] Llordés, A., Garcia, G., Gazquez, J., & Milliron, D. J. (2013). Nature, 500(7462), 323-326.

[28] Abb, M., Wang, Y., Papasimakis, N., de Groot, C. H., & Muskens, O. L. (2013). Surface-enhanced infrared spectroscopy using metal oxide plasmonic antenna arrays. *Nano letters*, *14*(1), 346-352.

[29] Adato, R., & Altug, H. (2013). In-situ ultra-sensitive infrared absorption spectroscopy of biomolecule interactions in real time with plasmonic nanoantennas. *Nature communications*, *4*.

[30] Dregely, D., Neubrech, F., Duan, H., Vogelgesang, R., & Giessen, H. (2013). Vibrational near-field mapping of planar and buried three-dimensional plasmonic nanostructures. *Nature communications*, *4*.

[31] Brown, L. V., Zhao, K., King, N., Sobhani, H., Nordlander, P., & Halas, N. J. (2013). Surface-enhanced infrared absorption using individual cross antennas tailored to chemical moieties. *Journal of the American Chemical Society*, *135*(9), 3688-3695.

[32] D'Andrea, C., Bochterle, J., Toma, A., Huck, C., Neubrech, F., Messina, E., Faziol, B., Marago, O. M., La Chapelle, M. L., Gucciardi, P. G. & Pucci, A. (2013). Optical nanoantennas for multiband surface-enhanced infrared and Raman spectroscopy. *ACS nano*, *7*(4), 3522-3531.

[33] Yazaydın, A. O., Benin, A. I., Faheem, S. A., Jakubczak, P., Low, J. J., Willis, R. R., & Snurr, R. Q. (2009). Enhanced CO2 adsorption in metal-organic frameworks via occupation of open-metal sites by coordinated water molecules. Chemistry of Materials, 21(8), 1425-1430.

[34] Dalgarno, S. J., Thallapally, P. K., Barbour, L. J., & Atwood, J. L. (2007). Engineering void space in organic van der Waals crystals: calixarenes lead the way. *Chemical Society Reviews*, *36*(2), 236-245.

[35] Millward, A. R., & Yaghi, O. M. (2005). Metal-organic frameworks with exceptionally high capacity for storage of carbon dioxide at room temperature. *Journal of the American Chemical Society*, *127*(51), 17998-17999.

[36] Cavenati, S., Grande, C. A., Rodrigues, A. E., Kiener, C., & Müller, U. (2008). Metal organic framework adsorbent for biogas upgrading. *Industrial & Engineering Chemistry Research*, *47*(16), 6333-6335.

[37] Kreno, L. E., Hupp, J. T., & Van Duyne, R. P. (2010). Metal– organic framework thin film for enhanced localized surface plasmon resonance gas sensing. *Analytical chemistry*, *82*(19), 8042-8046.

[38] Hermes, S., Witte, T., Hikov, T., Zacher, D., Bahnmüller, S., Langstein, G., Huber, K. & Fischer, R. A. (2007). Trapping metal-organic framework nanocrystals: an in-situ time-resolved light scattering

study on the crystal growth of MOF-5 in solution. *Journal of the American Chemical Society*, *129*(17), 5324-5325.

[39] Cho, W., Lee, H. J., & Oh, M. (2008). Growth-controlled formation of porous coordination polymer particles. *Journal of the American Chemical Society*, *130*(50), 16943-16946.

[40] Tsuruoka, T., Furukawa, S., Takashima, Y., Yoshida, K., Isoda, S., & Kitagawa, S. (2009). Nanoporous nanorods fabricated by coordination modulation and oriented attachment growth. *Angewandte Chemie International Edition*, *48*(26), 4739-4743.

[41] Cravillon, J., Münzer, S., Lohmeier, S. J., Feldhoff, A., Huber, K., & Wiebcke, M. (2009). Rapid room-temperature synthesis and characterization of nanocrystals of a prototypical zeolitic imidazolate framework. *Chemistry of Materials*, *21*(8), 1410-1412.

[42] Cravillon, J., Nayuk, R., Springer, S., Feldhoff, A., Huber, K., & Wiebcke, M. (2011). Controlling zeolitic imidazolate framework nano-and microcrystal formation: insight into crystal growth by time-resolved in situ static light scattering. *Chemistry of Materials*, *23*(8), 2130-2141.

[43] Pang, M., Cairns, A. J., Liu, Y., Belmabkhout, Y., Zeng, H. C., & Eddaoudi, M. (2012). Highly monodisperse MIII-based soc-MOFs (M= In and Ga) with cubic and truncated cubic morphologies. *Journal of the American Chemical Society*, *134*(32), 13176-13179.

[44] Umemura, A., Diring, S., Furukawa, S., Uehara, H., Tsuruoka, T., & Kitagawa, S. (2011). Morphology design of porous coordination polymer crystals by coordination modulation. *Journal of the American Chemical Society*, *133*(39), 15506-15513.

[45] Xu, X., Cao, R., Jeong, S., & Cho, J. (2012). Spindle-like mesoporous α-Fe2O3 anode material prepared from MOF template for high-rate lithium batteries. *Nano letters*, *12*(9), 4988-4991.

[46] Pan, Y., Heryadi, D., Zhou, F., Zhao, L., Lestari, G., Su, H., & Lai, Z. (2011). Tuning the crystal morphology and size of zeolitic imidazolate framework-8 in aqueous solution by surfactants. *CrystEngComm*, *13*(23), 6937-6940.

[47] Sindoro, M., Yanai, N., Jee, A. Y., & Granick, S. (2013). Colloidal-sized metal–organic frameworks: synthesis and applications. *Accounts of chemical research*, *47*(2), 459-469.

[48] Hermes, S., Schröder, F., Chelmowski, R., Wöll, C., & Fischer, R. A. (2005). Selective nucleation and growth of metal-organic open framework thin films on patterned COOH/CF3-terminated self-assembled monolayers on Au (111). *Journal of the American Chemical Society*, *127*(40), 13744-13745.

[49] Käfer, D., Witte, G., Cyganik, P., Terfort, A., & Wöll, C. (2006). A comprehensive study of

self-assembled monolayers of anthracenethiol on gold: Solvent effects, structure, and stability. *Journal of the American Chemical Society*, *128*(5), 1723-1732.

[50] Biemmi, E., Scherb, C., & Bein, T. (2007). Oriented Growth of the Metal Organic Framework $Cu_3(BTC)_2(H_2O)_3 \cdot xH_2O$ Tunable with Functionalized Self-Assembled Monolayers. *Journal of the American Chemical Society*, *129*(26), 8054-8055.

[51] Zacher, D., Baunemann, A., Hermes, S., & Fischer, R. A. (2007). Deposition of microcrystalline $[Cu_3(btc)_2]$ and $[Zn_2(bdc)_2]$ at alumina and silica surfaces modified with patterned self assembled organic monolayers: evidence of surface selective and oriented growth. *Journal of Materials Chemistry*, *17*(27), 2785-2792.

[52] Yoo, Y., & Jeong, H. K. (2008). Rapid fabrication of metal organic framework thin films using microwave-induced thermal deposition. *Chem. Commun.*, (21), 2441-2443.

[53] Yoo, Y., Lai, Z., & Jeong, H. K. (2009). Fabrication of MOF-5 membranes using microwave-induced rapid seeding and solvothermal secondary growth. *Microporous and Mesoporous Materials*, *123*(1), 100-106.

[54] Ameloot, R., Stappers, L., Fransaer, J., Alaerts, L., Sels, B. F., & De Vos, D. E. (2009). Patterned growth of metal-organic framework coatings by electrochemical synthesis. *Chemistry of Materials*, *21*(13), 2580-2582.

[55] Ameloot, R., Pandey, L., Van der Auweraer, M., Alaerts, L., Sels, B. F., & De Vos, D. E. (2010). Patterned film growth of metal–organic frameworks based on galvanic displacement. *Chemical communications*, *46*(21), 3735-3737.

[56] Schoedel, A., Scherb, C., & Bein, T. (2010). Oriented Nanoscale Films of Metal-Organic Frameworks By Room-Temperature Gel-Layer Synthesis. *Angewandtes Chemie International Edition, 49*(40), 7225-7228.

[57] Shekhah, O. (2010). Layer-by-Layer method for the synthesis and growth of surface mounted metal-organic frameworks (SURMOFs). *Materials*, *3*(2), 1302-1315.

[58] Shigesato, Y., Takaki, S., & Haranoh, T. (1992). Electrical and structural properties of low resistivity tin-doped indium oxide films. *Journal of Applied Physics*, *71*(7), 3356-3364.

[59] Dattoli, E. N., & Lu, W. (2011). ITO nanowires and nanoparticles for transparent films. *Mrs Bulletin*, *36*(10), 782-788.

[60] Hong, H. S., Jung, H., & Hong, S. J. (2010). Recycling of the indium scrap from ITO sputtering waste. *Research on Chemical Intermediates*, *36*(6-7), 761-766.

[61] Jeong, J. A., Lee, J., Kim, H., Kim, H. K., & Na, S. I. (2010). Ink-jet printed transparent electrode using nano-size indium tin oxide particles for organic photovoltaics. *Solar Energy Materials and Solar Cells*, *94*(10), 1840-1844.

[62] Li, S., Qiao, X., Chen, J., Wang, H., Jia, F., & Qiu, X. (2006). Effects of temperature on indium tin oxide particles synthesized by co-precipitation. *Journal of crystal growth*, *289*(1), 151-156.

[63] Yu, D., Wang, D., Yu, W., & Qian, Y. (2004). Synthesis of ITO nanowires and nanorods with corundum structure by a co-precipitation-anneal method. *Materials Letters*, *58*(1), 84-87.

[64] Gao, Z., Gao, Y., Li, Y., & Li, Y. (1999). Effects of heat treatment on the microstructure of nanophase indium-tin oxide. *Nanostructured materials*, *11*(5), 611-616.

[65] Nam, J. G., Choi, H., Kim, S. H., Song, K. H., & Park, S. C. (2001). Synthesis and sintering properties of nanosized In 2 O 3-10wt% SnO 2 powders. *Scripta materialia*, *44*(8), 2047-2050.

[66] Kim, K. Y., & Park, S. B. (2004). Preparation and property control of nano-sized indium tin oxide particle. *Materials Chemistry and Physics*, *86*(1), 210-221.

[67] Devi, P. S., Chatterjee, M., & Ganguli, D. (2002). Indium tin oxide nano-particles through an emulsion technique. *Materials Letters*, *55*(4), 205-210.

[68] Lee, J. S., & Choi, S. C. (2005). Solvent effect on synthesis of indium tin oxide nano-powders by a solvothermal process. *Journal of the European Ceramic Society*, *25*(14), 3307-3314.

[69] Sasaki, T., Endo, Y., Nakaya, M., Kanie, K., Nagatomi, A., Tanoue, K., Nakamura, R. & Muramatsu, A. (2010). One-step solvothermal synthesis of cubic-shaped ITO nanoparticles precisely controlled in size and shape and their electrical resistivity. *Journal of Materials Chemistry*, *20*(37), 8153-8157.

[70] Bühler, G., Thölmann, D., & Feldmann, C. (2007). One-Pot Synthesis of Highly Conductive Indium Tin Oxide Nanocrystals. *Advanced Materials*, *19*(17), 2224-2227.

[71] Jeon, M. K., & Kang, M. (2008). Synthesis and characterization of indium-tin-oxide particles prepared using sol–gel and solvothermal methods and their conductivities after fixation on polyethyleneterephthalate films. *Materials Letters*, *62*(4), 676-682.

[72] Ba, J., Fattakhova Rohlfing, D., Feldhoff, A., Brezesinski, T., Djerdj, I., Wark, M., & Niederberger, M. (2006). Nonaqueous synthesis of uniform indium tin oxide nanocrystals and their electrical conductivity in dependence of the tin oxide concentration. *Chemistry of materials*, *18*(12), 2848-2854.

[73] Toki, M., & Aizawa, M. (1997). Sol-gel formation of ITO thin film from a sol including ITO powder. *Journal of Sol-Gel Science and Technology*, *8*(1-3), 717-720.

[74] Choi, S. I., Nam, K. M., Park, B. K., Seo, W. S., & Park, J. T. (2008). Preparation and optical properties of colloidal, monodisperse, and highly crystalline ITO nanoparticles. *Chemistry of Materials*, *20*(8), 2609-2611.

[75] Sun, Z., He, J., Kumbhar, A., & Fang, J. (2010). Nonaqueous synthesis and photoluminescence of ITO nanoparticles. *Langmuir*, *26*(6), 4246-4250.

[76] Kanehara, M., Koike, H., Yoshinaga, T., & Teranishi, T. (2009). Indium tin oxide nanoparticles with compositionally tunable surface plasmon resonance frequencies in the near-IR region. *Journal of the American Chemical Society*, *131*(49), 17736-17737.

[77] Zarghami, M. H., Liu, Y., Gibbs, M., Gebremichael, E., Webster, C., & Law, M. (2010). p-Type PbSe and PbS quantum dot solids prepared with short-chain acids and diacids. *ACS nano*, *4*(4), 2475-2485.

[78] Garcia, G., Buonsanti, R., Runnerstrom, E. L., Mendelsberg, R. J., Llordes, A., Anders, A., Richardson, T. J. & Milliron, D. J. (2011). Dynamically modulating the surface plasmon resonance of doped semiconductor nanocrystals. *Nano letters*, *11*(10), 4415-4420.

[79] Gilstrap, R. A., Capozzi, C. J., Carson, C. G., Gerhardt, R. A., & Summers, C. J. (2008). Synthesis of a nonagglomerated indium tin oxide nanoparticle dispersion. *Advanced Materials*, *20*(21), 4163-4166.

[80] Jin, Y., Yi, Q., Ren, Y., Wang, X., & Ye, Z. (2013). Molecular mechanism of monodisperse colloidal tin-doped indium oxide nanocrystals by a hot-injection approach. *Nanoscale research letters*, *8*(1), 1-10.

[81] Lee, J., Lee, S., Li, G., Petruska, M. A., Paine, D. C., & Sun, S. (2012). A facile solution-phase approach to transparent and conducting ITO nanocrystal assemblies. *Journal of the American Chemical Society*, *134*(32), 13410-13414.

[82] Ohodnicki, P. R., Buric, M. P., Brown, T. D., Matranga, C., Wang, C., Baltrus, J., & Andio, M. (2013). Plasmonic nanocomposite thin film enabled fiber optic sensors for simultaneous gas and temperature sensing at extreme temperatures. *Nanoscale*, *5*(19), 9030-9039.

[83] Caruntu, D., Yao, K., Zhang, Z., Austin, T., Zhou, W., & O'Connor, C. J. (2010). One-step synthesis of nearly monodisperse, variable-shaped In2O3 nanocrystals in long chain alcohol solutions. *The Journal of Physical Chemistry C*, *114*(11), 4875-4886.

[84] Luo, S., Yang, D., Feng, J., & Ng, K. M. (2014). Synthesis and application of non-agglomerated ITO nanocrystals via pyrolysis of indium–tin stearate without using additional organic solvents. *Journal of nanoparticle research*, *16*(8), 1-12.

[85] Neouze, M. A., & Schubert, U. (2008). Surface modification and functionalization of metal and metal oxide nanoparticles by organic ligands. Monatshefte für Chemie-Chemical Monthly, 139(3), 183-195.

[86] Jung, L. S., Campbell, C. T., Chinowsky, T. M., Mar, M. N., & Yee, S. S. (1998). Quantitative interpretation of the response of surface plasmon resonance sensors to adsorbed films. Langmuir, 14(19), 5636-5648.

[87] Hunsche, A., Gorl, U., Muller, A., Knaack, M., & Gobel, T. (1997). Investigations concerning the reaction silica/organosilane and organosilane/polymer-Part 1: Reaction mechanism and reaction model for silica/organosilane. Kautschuk Gummi Kunststoffe, 50(12), 881-889.

[88] Haensch, C., Hoeppener, S., & Schubert, U. S. (2010). Chemical modification of self-assembled silane based monolayers by surface reactions. Chemical Society Reviews, 39(6), 2323-2334.

[89] Palma, R.D., Peeters, S., Van Bael, M. J., Van den Rul, H., Bonroy, K., Laureyn, W., Mullens, J., Borghs, G. & Maes, G. (2007). Silane ligand exchange to make hydrophobic superparamagnetic nanoparticles water-dispersible. *Chemistry of Materials*, *19*(7), 1821-1831.

[90] Roberts, J. J., Vuong, K. T., & Murray, R. W. (2012). Synthesis and Electrochemistry of 6 nm Ferrocenated Indium–Tin Oxide Nanoparticles. *Langmuir*, *29*(1), 474-479.

[91] Klokkenburg, M., Hilhorst, J., & Erne, B. H. (2007). Surface analysis of magnetite nanoparticles in cyclohexane solutions of oleic acid and oleylamine. *Vibrational spectroscopy*, *43*(1), 243-248.

[92] Shukla, N., Svedberg, E. B., & Ell, J. (2007). Surfactant isomerization and dehydrogenation on FePt nanoparticles. *Colloids and Surfaces A: Physicochemical and Engineering Aspects*, *301*(1), 113-116.

[93] Rahmelow, K., Hübner, W., & Ackermann, T. (1998). Infrared absorbances of protein side chains. *Analytical biochemistry*, *257*(1), 1-11.

[94] Kar, M., Agrawal, R., & Hillhouse, H. W. (2011). Formation pathway of CuInSe2 nanocrystals for solar cells. *Journal of the American Chemical Society*, *133*(43), 17239-17247.

[95] Barlow, S. M., Kitching, K. J., Haq, S., & Richardson, N. V. (1998). A study of glycine adsorption on a Cu {110} surface using reflection absorption infrared spectroscopy. *Surface science*, *401*(3), 322-335

[96] Launer, P. J. (1987). Infrared analysis of organosilicon compounds: spectra-structure correlations. *Silicone compounds register and review*, 100-103.

[97] Cabaniss, S. E., & McVey, I. F. (1995). Aqueous infrared carboxylate absorbances: aliphatic monocarboxylates. *Spectrochimica Acta Part A: Molecular and Biomolecular Spectroscopy*, *51*(13), 2385-2395

[98] Kelly, K. L., Coronado, E., Zhao, L. L., & Schatz, G. C. (2003). The optical properties of metal nanoparticles: the influence of size, shape, and dielectric environment. *The Journal of Physical Chemistry B*, *107*(3), 668-677.

[99] Miller, M. M., & Lazarides, A. A. (2005). Sensitivity of metal nanoparticle surface plasmon resonance to the dielectric environment. *The Journal of Physical Chemistry B*, *109*(46), 21556-21565.

[100] Jensen, T. R., Duval, M. L., Kelly, K. L., Lazarides, A. A., Schatz, G. C., & Van Duyne, R. P. (1999). Nanosphere lithography: effect of the external dielectric medium on the surface plasmon resonance spectrum of a periodic array of silver nanoparticles. *The Journal of Physical Chemistry B*, *103*(45), 9846-9853.

[101] Wang, Q. M., Shen, D., Bülow, M., Lau, M. L., Deng, S., Fitch, F. R., Lemcoff, N. O. & Semanscin, J. (2002). Metallo-organic molecular sieve for gas separation and purification. Microporous and mesoporous materials, 55(2), 217-230.

[102] Yazaydın, A. O., Benin, A. I., Faheem, S. A., Jakubczak, P., Low, J. J., Willis, R. R., & Snurr, R. Q. (2009). Enhanced CO_2 adsorption in metal-organic frameworks via occupation of open-metal sites by coordinated water molecules. Chemistry of Materials, 21(8), 1425-1430.

[103] Malinsky, M. D., Kelly, K. L., Schatz, G. C., & Van Duyne, R. P. (2001). Chain length dependence and sensing capabilities of the localized surface plasmon resonance of silver nanoparticles chemically modified with alkanethiol self-assembled monolayers. Journal of the American Chemical Society, 123(7), 1471-1482.

[104] Li, J. F., Huang, Y. F., Ding, Y., Yang, Z. L., Li, S. B., Zhou, X. S., Fan, F. R., Zhang, W., Zhou, Z. Y., Wu, Y. D., Ren, B., Wang, Z. L & Tian, Z. Q. (2010). Shell-isolated nanoparticle-enhanced Raman spectroscopy. nature, 464(7287), 392-395.

[105] Cavenati, S., Grande, C. A., Rodrigues, A. E., Kiener, C., & Müller, U. (2008). Metal organic framework adsorbent for biogas upgrading. Industrial & Engineering Chemistry Research, 47(16), 6333-6335.